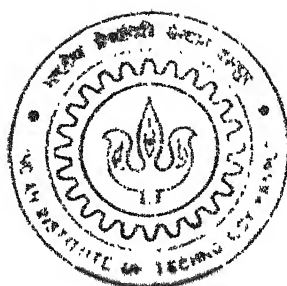# TOMOGRAPHIC TECHNIQUES AND SIMULATION OF HIGH DENSITY TWO-PHASE FLOWS FOR GAS-DRIVEN ADS TARGET SYSTEMS

By

Rajneesh Chaudhary

NUCLEAR ENGINEERING & TECHNOLOGY PROGRAMME

DEPARTMENT OF MECHANICAL ENGINEERING

INDIAN INSTITUTE OF TECHNOLOGY KANPUR

AUGUST, 2003

TOMOGRAPHIC TECHNIQUES AND SIMULATION OF HIGH DENSITY TWO-PHASE FLOWS FOR GAS-DRIVEN ADS TARGET SYSTEMS

A Thesis Submitted
in Partial Fulfillment of the Requirements
for the Degree of
Master of Technology

By
RAJNEESH CHAUDHARY

to the

NUCLEAR ENGINEERING & TECHNOLOGY PROGRAMME

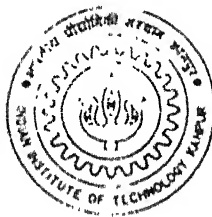DEPARTMENT OF MECHANICAL ENGINEERING
INDIAN INSTITUTE OF TECHNOLOGY KANPUR

Aug 2003

CERTIFICATE

It is certified that the work contained in the thesis entitled, *"Tomographic techniques and simulation of high density two-phase flows for gas-driven ADS target systems"* by **Rajneesh Chaudhary,** has been carried out under my supervision and that this work has not been submitted elsewhere for a degree.

Prof. P. Munshi

Department of Mechanical Engineering,

I.I.T. Kanpur

Aug 2003

DEDICATED

TO

MY BELOVED PARENTS

Abstract

Experimental Gamma-ray attenuation technique along with efficient tomographic inversion algorithms and two-fluid modeling, both are in use, to study the liquid metal two-phase flow intricacies since long.

The formulation for the chord average void-fractions from experimentally collected photon counts (Gamma-ray attenuation technique) and then their inversion to have line-by-line, point-by-point and simultaneous void distributions have been presented. Seven series expansion methods (Simple ART/Anderson ART/Gilbert ART/Gordon ART/GBH MART/GH MART/Lent MART) along with two optimization reconstruction techniques (MAXENT/MEM) have been implemented in FORTRAN-90. The performance of these methods has been checked over three field functions namely constant, step, and impulse. Five errors (average error/RMS error/normalized RMS error/maximum absolute error/normalized absolute error) have been reported. Plots of RMS error vs. relaxation parameter for all the algorithms except maximum entropy method have also been presented in step field reconstructions. The reconstructions corresponding to the relaxation parameter causing minimum RMS error have been presented.

Even with implications such as effort, cost and time of above discussed methodology (Gamma ray attenuation technique), it only gives the void fraction distributions at a particular cross-section without any information about fluid velocities, pressure etc.

Additionally, two-fluid modeling of liquid metal two-phase flows for the purpose of ADS (Accelerator Driven Sub-critical Reactor) development has been proposed. Formulation of Two-fluid model with proper constitutive laws for LBE (Lead-Bismuth Eutectic)-Argon system has been done. This is a six-equation model, having two sets of field equations, governing the process of conservation of mass, momentum, and energy. These six-equations have been solved by an extension of ICE (Implicit, Continuous, Eulerian) technique for single phase flows; this technique was named IMF (Implicit Multi-Field) for two-fluid calculations. Formulations for numerical solution have been done using finite difference technique with Eulerian cells and interfacial transfer terms

have been handled linear implicitly (though in actual sense, non-linearity exists). Implementation of the model has been carried out in FORTRAN-90 compiler.

Interfacial drag transport has been formulated from Ishii et al's work, however no entropy production at the interfaces and infinitely small interfacial thickness has been assumed to deal with interfacial heat transfer.

In the present work, a simple geometry has been taken into consideration for demonstration purpose with the possibility of the application of the two-fluid model in a gas-driven ADS target system. The two-fluid model has been solved for bubbly flow in undistorted particle regime. Void-fraction patterns along with gas and liquid velocities have been reported at four real time levels.

At last it can be said that all the above studies have been carried out to show the possibility of the application of the two techniques (Gamma-ray attenuation technique and Two-fluid modeling) on a gas driven ADS target system to have an insight of two-phase flow dynamics there.

Acknowledgements

CONTENTS

List of figures

List of tables

Nomenclature

a_g	isentropic acoustic velocity of gas
a_l	isentropic acoustic velocity of liquid
B_g	volume of a typical particle
C	specific heat
C_D	drag resistance coefficient
C_{VM}	virtual mass coefficient
D	discrepancy in continuity equation
f_j	field value or void fraction of jth cell
$\vec{F}_s$	standard drag force
$\vec{F}_v$	virtual mass force
g	acceleration due to gravity
$I(X)$	radiation intensity at thickness X
I_o	initial intensity of the radiation at the entrance into the investigated object
K	interfacial momentum transfer coefficient
K_l	liquid thermal conductivity
K_g	gas thermal conductivity
k	coefficient of bulk viscosity
L_i	chord length of ith ray
m_w	molecular weight
m	mass of the gas
M	number of rays
M_{ij}	number of rays passing through j^{th} cell
$\dot{M}_{ig}$	total interfacial gas momentum transfer
N	number of cells
P	pressure
P_i, α_i	i^{th} ray projection data
R	interfacial heat transfer coefficient
Re	Reynolds number
r_b	bubble radius
T	temperature
T_{lm}	temperature of Lead-bismuth eutectic
T_{ut}	temperature of Argon gas
u	velocity in x or r-direction
v	velocity in y or z-direction
$\vec{V}_l$	liquid velocity vector
$\vec{V}_g$	gas velocity vector

$\vec{V}_l$	$(\vec{V}_l - \vec{V}_g)$ relative velocity
$w_{i,j}$	the length of intersection of ith ray with j[th] cell
$\dfrac{D_g(\ )}{Dt}$	substantial derivative, $\dfrac{\partial(\ )}{\partial t} + \vec{V}_g \bullet \nabla(\ )$
μ	absorption coefficient
$\overline{\alpha}_i$	chord average void fraction
α_j	field value or void fraction of jth cell
λ	relaxation parameter
ρ	microscopic density
ρ'	macroscopic density
I	specific internal energy
λ_l	second coefficient of viscosity for liquid
λ_g	second coefficient of viscosity for gas
μ_l	liquid dynamic viscosity
μ_v	gas dynamic viscosity
α	void fraction
α^c	critical void fraction
μ_m	mixture viscosity
δt	time step
δz	space step in z direction
δr	space step in r direction
$\sigma_{\phi\phi}$	viscous stress tensor on Φ-plane in Φ-direction
σ_{rz}	viscous stress tensor on r-plane in z-direction
σ_{rr}	viscous stress tensor on r-plane in r-direction
σ_{zz}	viscous stress tensor on z-plane in z-direction
γ	$\dfrac{C_p}{C_t}$

Subscript

M	liquid metal
2Φ	two phase
$i\theta$	i[th] ray with θ projection angle
g	gas
l	liquid

Superscript

n	n[th] time level quantities

Superbar

$\ddot{A}$	n[th] and (n+1)[th] time averaged quantity

Chapter 1

Introduction

High-density two-phase flows are becoming important in many applications like LMMHD, ADS etc. Void fraction is one of the important parameters, which greatly influences the performance of these systems because of its direct relation with pressure variations. In LMMHD, two-phase flow is developed in the riser tube by introducing gas at the bottom to circulate the liquid metal through entire loop. So to design LMMHD accurate void fraction patterns need to be studied carefully over the entire length of the riser. Two-phase flows are difficult to analyze in wide range of systems. Void distributions are governed by complex interactions between two-phases, external boundaries and fluid properties. The distribution also depends upon the flow regimes like bubbly, churn, slug and annular. For point-by-point, simultaneous and average void fraction calculations at a particular cross-section in LMMHD riser leg, Munshi and Satyamurthy have already proposed gamma-ray attenuation technique with tomographic inversion techniques [1, 14, 15, and 16].

Gas driven ADS as suggested by many researchers, is one more device among utilizing liquid metal two-phase flows. The idea to use accelerator driven systems is not new. Over the past few decades, however, the motivation for its development has rapidly changed. Originally ADS was developed to produce fissile materials, namely ^{239}Pu from ^{238}U or ^{233}U from ^{232}Th in the Material Testing Accelerators project at the Lawrence Livermoore Radiation Laboratory at the end of the forties. This project was abandoned in 1952 when high grade uranium ores were discovered in the United States. In addition, the subsequent idea of exploiting the spallation process to transmute actinides and fission products directly turned out to be ineffective. The proton beam currents required (around 30 mA) were much larger than the most optimistic theoretical designs for an accelerator could achieve. Further discoveries in accelerator technology (also a product of the Strategic Defence Initiative - Star Wars program) have started a new wave of interest in using ADS. The accelerator generates high energy (around 1 GeV, current 0 and 30 mA) charged particles (e.g. protons) which strike a heavy material target. This bombardment

1

the production of a very intense neutron source, producing spallation neutrons typically in the range of 10^{18} per second (a process called spallation) [10, 17]. These neutrons enter a subcritical core (often called a blanket) where they can be multiplied. Reactor with ADS technology operates under sub-critical condition with high level of inherent safety, minimum waste production, and can utilize fertile components more efficiently [19].

Spallation nuclear reactions occur when an energetic projectile (E/A > 100 Mev/nucleon) hits a nucleus. This reaction can be seen as breaking of a nucleus into smaller parts in form of nucleons and clusters. The resulting heavy nuclear residues are also highly excited and emit a large number of nucleons (basically neutrons) by evaporation process. The Schematic of basic spallation process is given in Fig-1.1.
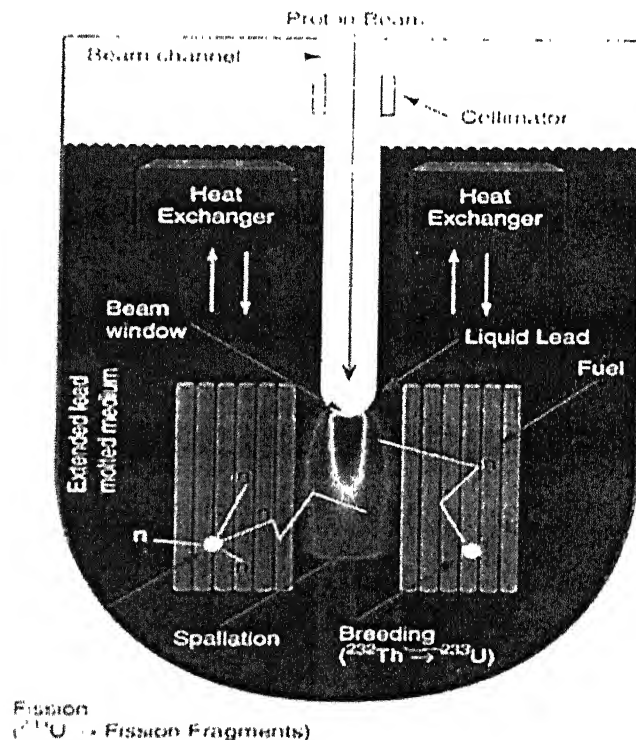
Fig-1.1 Schematic of a typical ADS reactor

For efficient production of neutrons, the most effective range of incident particles like protons is between 1 to 1.5 GeV and the figure of merit for neutron production is defined as the number of neutrons emitted per unit amount of energy deposited in the target [10]. Spallation target module is one of the important innovative components of the ADS. It constitutes the physical interface between the accelerator and the sub critical core, is

simultaneously subjected to severe thermal-mechanical loads and damage due to high-energy heavy particles (proton beam, spallation neutrons, and spallation products). The spallation module design should be based on balanced optimization among neutron yield, material properties and thermal-hydraulic performance under the required safety and reliability conditions [10].

One more important part of developing ADS is choosing a suitable target for desired performance. Out of various possible options under severe operational conditions, like high heat deposition by proton beam, by spallation products and by spallation neutrons Satyamurthy et al proposed lead bismuth eutectic (LBE, 45 % lead and 55 % bismuth) to utilize at target [10]. It has low melting point 123 $^\circ$C and also reduces the hazard of polonium gas, forming lead polonide [19].

One can have the same liquid acting as reactor coolant, and spallation target (valid for fast core). Alternatively, a separated loop for both of them can also be considered. In separated loop systems, two schemes are wide spread, window or windowless target systems [26-28]. In the window concept spallation heavy metal target and proton beam pipe (vacuum environment) are separated by solid window barrier through which the proton passes to interact with the target. The alternative concept is windowless, where the interface is the free surface of the liquid metal spallation target. Latter is only possible with LBE or Lead, because of their low vapour pressures at the operating temperatures ($< 500^\circ C$) [10].

High heat deposition in the liquid metal target occurs because of the proton beam interactions; therefore this heat should be carried away prior to the safety and corrosion limits. Various types of ADS schemes have been proposed consisting of fast, thermal, and fast thermal cores with different fuel compositions and different coolant schemes [19-25]. Mainly, three schemes are popular, natural convection, forced convection (mechanical pump driven conditions), and buoyancy driven enhanced by gas injection [22]. Above mentioned schemes together with their implementation and operating complicacies have been extensively discussed.

In buoyancy driven systems volumetric expansion coefficient of lead or LBE with high boiling temperature helps to circulate the lead or LBE. The heat deposition by proton beam raises the temperature of spallation zone and temperature of cold leg is maintained

using a heat exchanger. Higher the temperature difference between spallation zone and cold leg, higher is the flow rate, but if temperature difference exceeds a certain limit then it causes severe problem of corrosion in the module [29]. Though these systems are passively safe but at the same time they have two main disadvantages, namely, required target loop size is very large and shooting of coolant temperature at start up. To get rid of over shooting at the start up gas injection can be used. Fig-1.2 demonstrates simple buoyancy driven ADS target system.

Coupling flange
Coolant outlet
Coolant inlet

Proton beam pipe

Heat exchanger

Hot rising liquid metal

Cold descending liquid metal

Window
Spallation region

Flow guide
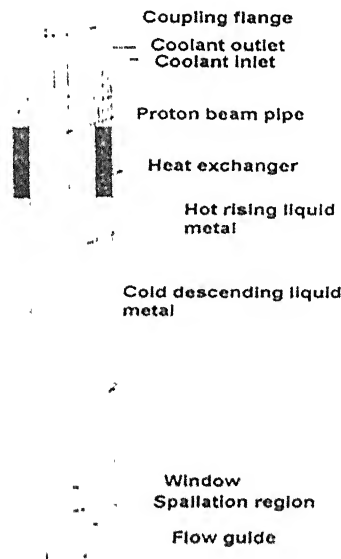
Fig-1.2 Buoyancy driven target module

Although, high flow velocities of heavy liquid metals, limits the degree of compactness, forced convection systems can be developed with lots of flexibility and compactness. EM (electromagnetic) pumps are more favorable than ordinary centrifugal pumps.

Third scheme is Buoyancy driven enhanced with gas injection systems (Fig-1.3) [27]. An inert gas is injected to enhance the buoyancy driven flow in these systems. The injected gas creates density difference between the two legs that leads to an induced pressure difference, which helps to circulate the liquid metal through target module. A heat exchanger is used to under limit the operating temperature of cold leg. The inert gas is separated out in separator tank located at the top of the module. This system reduces the liquid metal inventory and the size of natural circulation system. The need of maintenance of the inline dynamic machinery like pump is avoided and also the risk of

temperature overshooting at the start up is reduced. Fig-1.3 gives the details of a gas enhanced ADS target module.

Coupling flange
Coolant out
Coolant in
Separator
Gas
Proton beam
Heat exchanger
Mixer
Window
Spallation region
Flow guide
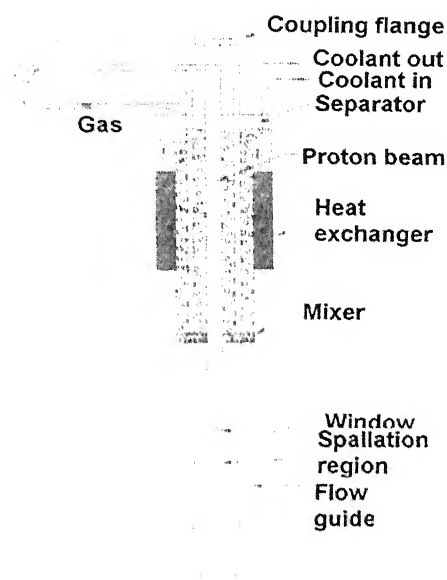
Fig-1.3 Gas enhanced or gas-driven target module

The studies of liquid metal two phase flows are carried out keeping in mind the development of gas enhanced buoyancy driven window type ADS. The performance of these systems crucially depends upon the two-phase flow dynamics and void fraction distributions.

Two of various available techniques for two-phase flow studies are considered here, first is the Gamma ray attenuation method to calculate chord average void-fractions then their inversion using tomographic techniques (ART/MART/MENT/MEM) in point-by-point and simultaneous void distributions. [1, 30-45]. This method suffers certain limitations; it can give void-fractions at a particular cross-section without any knowledge about pressure and velocities moreover experimental projection data is required, which is an expensive and time taking activity.

Additionally, two-fluid model has been used to have an insight of actual liquid metal two-phase flow fluctuations [2,8].

1.1 Review of literature

A review of the existing literature on studies related to ADS, tomographic techniques, and two-fluid modeling has been presented here. First part deals with the on going research over ADS technology, secondly advancements in tomographic techniques and lastly two-phase flow modeling.

Satyamurthy and Venkatramani (2002) [10] presented a state-of-art review of the ADS technology and developments. ADS studies have been taken up in view of their inherent safety and ability to utilize thorium and to transmute present nuclear waste. The main thermal-hydraulic feature of the target, heat deposition by proton beam has been thoroughly studied. Various issues related to thermal-hydraulics of window and windowless configurations based on buoyancy as well as gas-driven systems have been presented. The parameters of the target of 1.75 MW (proton beam of 350 MeV and 5 mA current) of the demonstration ADS reactor based on quasi-one-dimensional codes have been done along with the necessity to develop 2-D/3-D flow models for spallation flow region and the free surface flow in the case of windowless configuration. Finally, the conceptual design of an experimental LBE facility to be set up for validating the CFD codes for target loops for both window and windowless configuration has been presented.

Satyamurthy and Biswas (2002) [17] presented an interesting study on the thermal hydraulics of ADS systems. Preliminary thermal-hydraulic studies carried out on the spallation target of window type ADS based on LBE, with a thermal power of 100 MW in the fast zone have been discussed. The studies have been carried out both for buoyancy as well as gas driven target systems and complete analysis of the loop consisting of spallation region, riser, and two-phase flow region of the riser (for gas-driven target) heat exchanger, downcomer etc has been done. Parametric analysis for different flow rates, beam current (2 and 3 mA and 1 GeV), geometry etc have been presented and comparison has been made between buoyancy and gas-driven systems.

Radon (1917) [50], gave the idea of reconstructed a function from its projections. In the strict sense of word, a projection at a given angle is the integral of the image in the direction specified by that angle.

Hounsfield's (1973) [39] invention of the x-ray computed tomographic scanner for which he received a Nobel Prize in 1972 [4]. Hounsfield used algebraic techniques, like ART/MART.

Ramachandran and Lakshminarayan (1970) [38] developed a new method Convolution Back Projection. These algorithms considerably reduced the processing time for reconstruction, and the image produced was numerically more accurate. Convolution eliminates the step of computing Fourier transform and then its inverse so requires less computing time.

Gordon et al (1970) [33] presented an entirely different approach for tomographic imaging consists of assuming that the cross-section consists of an array of unknowns, and then setting up algebraic equations for the unknowns, in terms of the measured projection data. These techniques are very helpful when it is not possible to measure large number of projections and the projections are not uniformly distributed. These techniques are known as Series Expansion Methods or Algebraic Reconstruction Techniques/Multiplicative Reconstruction Technique.

Kak and Slaney in their book ", *Principles of Computerized Tomographic Imaging, IEEE Press, 1988*", presented a brief discussion over various tomographic techniques. Algebraic reconstruction techniques (ART) are discussed in detail in its 7th chapter and suggested, although conceptually this approach is much simpler than the transform based methods, for medical applications it lacks the accuracy and speed of implementation. However, there are situations where it is not possible to measure a large number of projections, or the projections are not uniformly distributed over 180 or 360 ^{0}, techniques like ART can be used effectively.

Gull and Newton (1986) [31] suggested many functions that can be extremized to have a realistic solution of reconstruction problem. The two functions that look attractive are

entropy and energy. First gives maximally unbiased and latter gives maximally biased solution.

Subbarao at el (1996) [30] thoroughly studied the performance and convergence of various series expansion and optimization reconstruction techniques. Algorithms used are mainly divided in three groups, namely the additive algebraic reconstruction technique (ART), the multiplicative algebraic reconstruction technique (MART) and the optimization reconstruction techniques. Additive ART algorithms have shown a systematic convergence with respect to number of projections and the value of relaxation parameter. MART algorithms have been found producing less error at convergence compared to additive ART but converge only at small values of relaxation parameters. Increasing noise level in projection data increase the error in reconstructed field and decrease the convergence rate.

Biswas and Munshi (2001) [1] applied ART algorithms over experimentally collected projections on LMMHD experimental facility available in BARC. First ART algorithms had been implemented over simulated data thereafter experimentally collected corrupted chord average void fractions were inverted to have void distributions.

Stewart and Wendroff (1984) [46] presented the basic principles of two-phase flow modeling and discussed about the ill posed ness of various wide spread models.

Ishii (1975) [2] presented an interesting formulation of two-fluid model. It was said that two-phase flow suffers interfacial discontinuities to over come these he presented interfacial jump conditions. Later in 1984, Ishii and Mishima [8] had presented interfacial drag formulations and interfacial area calculations with their general applications.

Liles and Reed (1978) [51] developed a new technique, semi-implicit method, for solving the equations of two-phase flow dynamics. Although its applicability over several sets of equations representing two-phase flows, including two-fluid model had been proposed, but they demonstrated the numerical technique for one-dimensional drift-flux model. Few

8

advantages of this technique over other techniques had also been reported, like stability, ease for complicated flow networks, and ease of extension to problems in two or three dimensions.

Harlow and Amsden (1971) [3] revised the ICE (Implicit Continuous-field Eulerian) technique and generalized for the arbitrary equation of state and full viscous stress tensors. It was said that this method is useful for the numerical solution of time-dependent fluid flow problems in several space dimensions, for all Mach numbers from zero (incompressible limit) to infinity (hypersonic limit).

Hirt, Amsden and Cook (1974) [51] given a brief theory of a technique similar to ICE with finite difference formulations over three kind of cells, namely Lagrangian (vertices can be moved with the fluid), Eulerian (to be held fixed) and be moved in any other prescribed manner. Their publication describes the basic methodology, finite difference approximations, and discussions about stability, accuracy and zoning.

Harlow and Amsden (1975) [4] had presented the simplified and extended form of IMF (Implicit Multi-field Technique, an extension of ICE for two-phase flow calculations) on momentum coupling among fields. The extensions included the capability for compressibility in each material phase, the addition of more interpenetrating fields, and allowance for the motion of liquid or vapor through a close-packed field of particles. The technique had been illustrated by computer generated plots from time varying three-field calculation in a cylindrically.

Harlow and Amsden (1975) [7] proposed a new technique analogous to ICE for numerical solution of two-fluid model (IMF), in which several fields interpenetrate and interact with each other. An implicit coupling for each field between mass transport and equation of state allowed calculations in all flow-speed regimes, from far subsonic (incompressible) to far supersonic. In addition, the momentum transport between fields was coupled implicitly, allowing for all degrees of coupling, from very loose to completely tied together. Considerable generality has been presented, to permit

application to wide scope of complicated problems, for example, the fluidized dust bed, the flow of a liquid with entrained bubbles, and atmospheric condensation with the fall of precipitation.

Stewart (1979) [5] presented a study of stability on two-fluid modeling, it was said a two-fluid modeling may yield a system of partial differential equations having complex characteristics; this results in a mathematically ill-posed initial-value problem. Despite that fact that no finite-difference method for solving such a problem can be stable in the usual sense, finite difference solution of the two-fluid model is in wide spread use. He investigated the numerical behavior of one such set of difference equations, derived conditions under which solutions appeared to be well behaved, and offered a physical interpretation.

1.2 Objective of the present work

Two-phase flow dynamics crucially depend upon the void fraction distributions. Munshi et al (1997) [1, 15] suggested iterative tomographic algorithms for the inversion of corrupted projection data, collected using gamma ray attenuation technique to calculate line-by-line, point-by-point and simultaneous void fraction distributions. A FORTRAN-90 code has been developed for series expansion and optimization reconstruction algorithms, to check their performance over three simulated functions namely constant, step, and impulse with a motive to apply these algorithms over ADS leg. Mainly five errors have been calculated in order to check their performance for the application over an ADS leg, the range of relaxation parameter of all the algorithms with step reconstructions has been reported, different relaxation parameter reconstruct different features of a simulated data. If one algorithm shows divergence for some value of relaxation parameter then it can be concluded that the algorithm is not capable to reconstruct the features corresponding to the concerned relaxation parameter. The features corresponding to minimum RMS error are most desirable for better locally spread reconstructions thus all the reconstructions have been presented corresponding to the relaxation parameter having minimum RMS error.

For the same two-phase flow studies, two-fluid model has been formulated to study the liquid metal two-phase flow's complex microphysics in pure bubbly flow under viscous regime with appropriate analytical models for drag force [2, 8, 12]. The finite difference discretized equations have been solved using IMF (implicit multi-field technique) technique, an extension of ICE (implicit continuous technique) of single-phase flows [3, 4]. Convection terms have been discretized using partial donor cell differencing. A FORTRAN 90 code is developed for the numerical solution.

In the present work six field equations are solved for demonstration purpose over a simple geometry in bubbly flow under viscous regime. Liquid and gas velocity vectors along with void fraction contour are plotted.

The tomographic algorithms and transient two-dimensional two-fluid model have been developed in the present work, keeping in mind the two-phase flow studies for the design and development of gas-driven accelerator driven systems.

1.3 Structure of the thesis

Chapter 2 presents an analytical study of projection data calculations from experimentally collected photon counts and discussions about various tomographic algorithms. Chapter 3 deals with the mathematical formulations of the possible algorithms for incomplete data reconstructions (series expansion and optimization algorithms). In Chapter 4 the reconstructions of three simulated projection data with five errors, profiles of RMS error vs. relaxation parameter, and discussions over results have been carried out. Chapter 5 has been devoted to the formulations of transient two-dimensional two-fluid model along with interfacial drag, discussions about stability, and applicability on a LBE-Argon system. Chapter 6 has been devoted to results and discussions over two-fluid simulations of an LBE-Argon system; velocity vectors and void fraction profiles have also been presented. At last, in Chapter 7 conclusions and future scope of the present work have been presented.

Chapter 2

Reconstruction algorithms and theoretical approach

Image reconstruction from projection can be viewed as linear inverse problem with discrete data. Reconstruction can be achieved mainly by four ways, direct matrix inversion, transform methods (Fourier and Hilbert transform), filtered convolution back projection methods, and ART. Among all discussed Convolution Back Projection Algorithm is used extensively [37-38]. Convolution Back Projection requires data for a large number of angles and should be uniformly distributed to have an exact inversion. However in many practical cases it might not be possible to have such large data. On the other side, with limited data tomography encounters ill-posed problem in reconstruction. To overcome these tomographic problems Series Expansion Methods have been proposed, like Additive ART/ Multiplicative ART [33, 39 and 40]. As in the conventional ART methods, additive or multiplicative corrections are possible in all the algorithms, which belong into ART family. Recent studies have indicated that, of the several classes of reconstruction algorithms applicable to limited data, those based on multiplicative algebraic reconstruction (MART) are the fastest, most flexible and accurate. Verhoeven presented various types of MART algorithms and applied them for interferometer data [40].

Reconstruction may be defined ill posed based upon two logics, incomplete data and noisy data. Being ill-posed problem in reconstruction with incomplete and noisy data, there are many feasible solutions, which are consistent with the data. It is a matter of practical necessity to select a single solution from the feasible set. The Maximum Entropy method consists of choosing a single feasible solution, which has maximum configurationally entropy, means it is maximally noncommittal about unmeasured parameters. Gull and Newton suggested many functions those can be extremized to have a realistic solution to reconstruction problem [31]. The two functions those look attractive are entropy and energy. First gives maximally unbiased and latter gives maximally biased solution.

Presently focus has been kept on series expansion and optimization methods. All the methods are iterative in nature, Gordon first proposed ART algorithm with name Gordon ART for CT images [33]. Later Gilbert developed a form of ART called simultaneous iterative reconstruction technique (SIRT) [34]. After this Anderson and Kak combined ART and SIRT and gave a new name to this, simultaneous algebraic reconstruction technique (SART) [35]. In later 1990's Mayinger opted a simplest reconstruction algorithms for reconstructions, Simple ART [32].

With these additive correction algorithms, multiplicative correction algorithms are also proposed for ill-posed problems. First Gordon et al (1970) proposed GBH MART [33]. Later Gordon and Herman (1974) proposed a slight difference in correction and named this algorithm GH MART [41]. Lent (1977) proposed another multiplicative algorithm Lent MART [36]. And it was reported that multiplicative algorithms are better and efficient for ill-posed problems.

2.1 Theoretical approach for chord average void-fractions

Projection of a field in a given direction can be seen as the line integral of the attenuation coefficient (μ) of the two-phase flow field. Interaction of matter with alpha and beta particles is a multiple collision process, however with Gamma rays it is only one-shot process. This directly leads to the exponential absorption law for Gamma rays, namely,

$$I(X) = I_0 e^{-\mu X} \tag{2.1}$$

Here, $I(X)$ is the intensity at thickness X, and μ, the total absorption coefficient. I_0, is initial intensity of the radiation at the entrance into the investigated volume.

Fig-2.1 shows the photon count collection at a cross-section on a pipe under liquid metal two-phase flow.
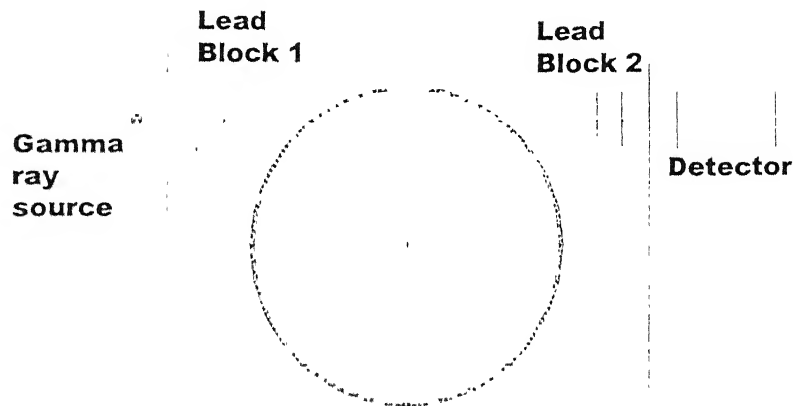
Fig-2.1 Projection data collection

Neglecting the attenuation coefficient of air, I_M, is the number of counts per unit second collected at the detector end when only liquid metal is flowing through the pipe. $I_{2\phi}$, is under the presence of mercury-nitrogen two-phase flow in the pipe. I_A, is the counts per second when nitrogen or air is only present in the pipe. Whereas μ_1, X_1, μ_2, X_2, μ_3, X_3, μ_4, X_4, are attenuation coefficient and thickness for lead block 1, liquid metal, lead block 2, and pipe material respectively.

Now,

$$X = X_1 + X_2 + X_3 + X_4$$

$$I_{2\phi_0} = I_{M_0} = I_{A_0} \tag{2.2}$$

$$I_M(X) = I_{M_0} e^{-\mu_1 X_1 - \mu_2 X_2 - \mu_3 X_3 - \mu_4 X_4} \tag{2.3}$$

$$I_{2\phi}(X) = I_{2\phi_0} e^{-\mu_1 X_1 - (1-\alpha)\mu_2 X_2 - \mu_3 X_3 - \mu_4 X_4} \tag{2.4}$$

$$I_A(X) = I_{A_0} e^{-\mu_1 X_1 - \mu_3 X_3 - \mu_4 X_4} \tag{2.5}$$

14

Now by equations (2.2), (2.3), and (2.4),

$$\frac{I_M(X)}{I_{2\Phi}(X)} = e^{-\bar{\alpha}\mu_2 X_2}$$

(2.6)

Now by equations (2.2), (2.3), and (2.5),

$$\frac{I_M(X)}{I_A(X)} = e^{-\mu_2 X_2}$$

(2.7)

Using equations (2.6) and (2.7),

$$\bar{\alpha}_c = \frac{\ln\left(\dfrac{I_{2\Phi}(X)}{I_M(X)}\right)}{\ln\left(\dfrac{I_A(X)}{I_M(X)}\right)}$$

(2.8)

Where, $\bar{\alpha}_c$, is the chord average void fraction.

Projection input for the series expansion optimization algorithms can be calculated by multiplying the chord average void fraction by chord length.

$$P_i = \bar{\alpha}_i = \bar{\alpha}_c \times L_i$$

(2.9)

Two-dimensional Field is divided into square cells, and cells are numbered in a regular fashion from bottom to top. The void fraction is assumed to be constant throughout a cell (i.e. α_j, is the void fraction of jth cell). In the present analysis, source, detector, and rays are considered ideal. The length of intersection of ith ray and j^{th} cell, denoted by $w_{i,j}$ for $i = 1, 2 \dots M$ and $j = 1, 2 \dots N$ represent the contribution of jth cell to the total void fraction along the ith ray.

Schematic of the discretization of the physical domain has been presented in Fig-2.2,

N

Detector

ith ray

1 2 3

Source

$W_{i,j}$
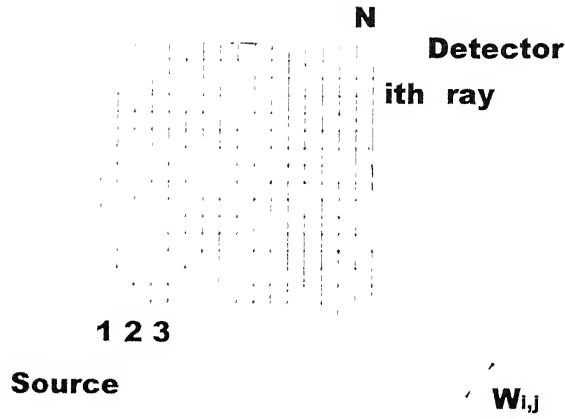
Fig-2.2 Discretization of field

By accounting the contribution of each cell into the average void fraction along a ray, the result is the system of linear equations.

$$P_i = \bar{\bar{\alpha}}_i = \sum_{l=1}^{N} w_{i,l} \, \alpha_l \qquad (2.10)$$

Or,

$$[W][\alpha] = [\bar{\alpha}] = [P] \qquad (2.11)$$

If M and N were small, conventional matrix theory methods would have been used to invert the system of equations. However, in practice M and N are large enough which precludes any possibility of direct matrix inversion. Of course, when noise is present in the projection data, and when M≪N, even for small N it's quite difficult to use direct inversion method; some least square methods may have been used. But when M and N are large, such methods are also impractical. Some iterative methods like ART/MART and optimization methods can be used for the inversion of the above problem.

Chapter 3

Mathematical formulations for reconstructions

The incomplete projection data leads to the application of series expansion and optimization methods for the present work. Additive as well as multiplicative correction algorithms have been studied. Optimization methods (maximum entropy and minimum energy methods) have also been used and results thus obtained are compared to report the best algorithm among all the available algorithms for the constant, step and impulse field reconstructions. The MART algorithms have shown their convergence to optimization algorithms with a necessary condition that the feasible set of solution, which satisfies the projection data, should be nonempty, means projections should not be corrupted [43, 44]. Consider a Cartesian grid of rectangular elements, introduced in a filled layer over a horizontal plane. Field parameters to be constructed are denoted by f_j, $j = 1,\ldots\ldots\ldots, N$.

The ith projection, which is a path integral, is approximated as

$$P_i = \overline{\alpha_i} = \sum_{j-1}^{N} w_{i,j} f_j \qquad i = 1,\ldots\ldots\ldots, M \qquad (3.1)$$

The weight function $w_{i,j}$ is defined as the length of intersection of the ith ray with the jth pixel. It can be seen that there are N unknowns that need to be solved from M equations. The resulting matrix $[w_{i,j}]$ is highly sparse and rectangular with size $M \times N$. And the problem can be viewed as developing generalized inverse of the matrix $[w_{i,j}]$, while obtaining the field values f_j.

The statements for algorithms with additive corrections are given first, followed by multiplicative correction algorithms and at last optimization methods have been presented.

3.1 Additive ART

3.1.1 Simple ART

Simple ART step by step is as follows [32],

1. initialization $f^0 \in R^n$ is arbitrary.

do for each iteration k.

do for each angle of projection θ.

    do for each ray i_θ

      a. compute the correction $\left((\bar{\alpha}_{i\theta})_{exp} - (\bar{\alpha}_{i\theta})_{theo} \right)$

      b. compute the total value of weight function along each ray,

$$W^r_{i\theta} = \sum_{l=1}^{N} w_{i\theta,l}$$

      c. calculate the average weight function $\dfrac{(\bar{\alpha}_{i\theta})_{exp} - (\bar{\alpha}_{i\theta})_{theo}}{W_{i\theta}}$.

    end do

  do for each ray i_θ

      a. update the each field parameter as

$$f_i^{new} = f_i^{old} + \lambda \frac{w_{i\theta,l} \left((\bar{\alpha}_{i\theta})_{exp} - (\bar{\alpha}_{i\theta})_{theo} \right)}{W_{i\theta}}$$

  end do

  do for each ray i_θ

      a. update the approximate projections using

$$(\bar{\alpha}_{i\theta})_{theo} = \sum_{p=1}^{N} w_{i\theta,l} f_i, \quad i_\theta = 1, \ldots \ldots, M_\theta$$

end do

end do

$$\text{a. stop when } \mathrm{abs}\left(\frac{\left(f_i^{K+1} - f_i^{K}\right)}{f_i^{K}}\right) \times 100 \leq 0.01$$

end do

3.1.2 Gordon ART

In this method corrections are applied to all the cells through which i^{th} ray passes, before calculating the correction for the next ray. Hence, the number of rays per angle of irradiation is not important [33].

1. initialization $f^0 \in R^n$ is arbitrary.

do for each iteration k

    do for each ray i

        a. compute the correction $\left(\left(\bar{\alpha}_i\right)_{exp} - \left(\bar{\alpha}_i\right)_{theo}\right)$

        b. compute the correction coefficient

$$c_i = \sum_{j=1}^{N} w_{i,j}^2$$

        c. apply a correction to each cell j of the test field through which the present ray passes as

$$f_i^{new} = f_i^{old} + \lambda \frac{w_{i,j}\left(\left(\bar{\alpha}_i\right)_{exp} - \left(\bar{\alpha}_i\right)_{theo}\right)}{c_i}$$

end do

    a. stop when **abs**$\left(\frac{\left(f_i^{K+1} - f_i^{K}\right)}{f_i^{K}}\right) \times 100 \leq 0.01$

    b. compute projection numerically

$$\left(\bar{\alpha}_i\right)_{theo} = \sum_{j=1}^{N} w_{i,j} f_j, \quad i = 1,\ldots\ldots\ldots, M$$

end do

3.1.3 Gilbert ART

This method is also known as SIRT (simultaneous iterative reconstruction technique). In SIRT, the elements of the field function are modified after all the correction values corresponding to individual rays have been calculated [34].

1. initialization $f^0 \in R^n$ is arbitrary.

do for each iteration k

    do for each ray i

        a. compute the correction $\left((\bar{\alpha}_i)_{exp} - (\bar{\alpha}_i)_{theo} \right)$

        b. compute the correction coefficient

$$c_i = \sum_{i=1}^{N} w_{i,i}^2$$

  end do

  do for each ray i

        a. identify all the rays, $M_{i,i}$ passing through a given cell and the corresponding $w_{i,i}$ and $\left((\bar{\alpha}_i)_{exp} - (\bar{\alpha}_i)_{theo} \right)$.

        b. apply a correction to each cell j of the test field through which the present ray passes as

$$f_i^{new} = f_i^{old} + \sum_{i=1}^{M_{i,i}} \lambda \frac{w_{i,i}\left((\bar{\alpha}_i)_{exp} - (\bar{\alpha}_i)_{theo} \right)}{c_i}$$

  end do

        a. stop when $\mathbf{abs}\left(\frac{\left(f_i^{K+1} - f_i^{K} \right)}{f_i^{K}} \right) \times 100 \leq 0.01$

        b. compute projection numerically

$$(\bar{\alpha}_i)_{theo} = \sum_{j=1}^{N} w_{i,i} f_i, \quad i = 1,\ldots\ldots, M$$

  end do

3.1.4 Anderson ART

This algorithm combines the ART and SIRT algorithms. Method of applying correction is similar to SIRT but the structure is similar to ART [35].

1. initialization $f^0 \in R^n$ is arbitrary.

do for each iteration k.

do for each angle of projection θ .

    do for each ray i_θ

      a. Compute the correction $\left(\left(\alpha_{i\theta} \right)_{exp} - \left(\overline{\alpha}_{i\theta} \right)_{theo} \right)$

      b. Compute the total value of weight function along each ray,

$$c_{i\theta} = \sum_{j=1}^{N} w_{i\theta,j}^{2}$$

    end do

    do for each ray i_θ

      a. update the each field parameter as

$$f_i^{new} = f_i^{old} + \lambda \frac{w_{i\theta,j} \left(\left(\alpha_{i\theta} \right)_{exp} - \left(\overline{\alpha}_{i\theta} \right)_{theo} \right)}{c_{i\theta}}$$

    end do

    do for each ray i_θ

      a. update the approximate projections using

$$\left(\overline{\alpha}_{i\theta} \right)_{theo} = \sum_{j=1}^{N} w_{i\theta,j} f_j, \quad i_\theta = 1,\ldots\ldots\ldots, M_\theta$$

    end do

  end do

  a. stop when **abs** $\left(\frac{\left(f_i^{K+1} - f_i^{K} \right)}{f_i^{K}} \right) \times 100 \leq 0.01$

end do

3.2 Multiplicative ART

When the correction is multiplicative, the ART is called multiplicative ART (MART) [33, 40 and 41].

1. Initialization $f^0 \in R^n$ is arbitrary.

do for each iteration k

  do for each ray i

  a. Identify all the rays, M_{cj} passing through a given cell and the corresponding $w_{i,j}$, $(\alpha_i)_{exp}$, and $(\overline{\alpha}_i)_{theo}$.

  b. Apply a correction to each cell j of the test field through which the present ray passes as

3.2.1 GBH MART

$$f_i^{new} = f_i^{old} \times \prod_{i=1}^{M_{cj}} \left[1 - \lambda \left(1 - \frac{(\overline{\alpha}_i)_{exp}}{(\overline{\alpha}_i)_{theo}} \right) \right]$$

3.2.2 GH MART

$$f_i^{new} = f_i^{old} \times \prod_{i=1}^{M_{cj}} \left[1 - \lambda \frac{w_{i,j}}{w_{max}} \left(1 - \frac{(\overline{\alpha}_i)_{exp}}{(\overline{\alpha}_i)_{theo}} \right) \right]$$

3.2.3 Lent MART

$$f_i^{new} = f_i^{old} \times \prod_{i=1}^{M_{cj}} \left[\frac{(\alpha_i)_{exp}}{(\overline{\alpha}_i)_{theo}} \right]^{\frac{\lambda w_{i,j}}{w_{max}}}$$

end do

  a. top when $abs\left(\frac{\left(f_i^{K+1} - f_i^{K} \right)}{f_i^{K}} \right) \times 100 \le 0.01$

  b. compute projection numerically

$$\overline{\alpha}_i = \sum_{j=1}^{N} w_{i,j} f_j \quad i = 1, \ldots \ldots \ldots, M$$

end do

3.3 Optimization techniques

3.3.1 Maximum entropy method

The probability of finding a system in a given state depends upon the multiplicity of that state. That is to say, it is proportional to the number of ways you can produce that state. Here a "state" is defined by some measurable property, which would allow you to distinguish it from other states. A greater value of multiplicity of state implies greater possibility of the system in that state. Based on the above-mentioned definition of entropy a tomographic algorithm is developed by Gull and Newton [31]. This method produces an unbiased solution and is maximally non-committal about unmeasured parameters. A formulation for the present algorithm is given as.

Maximum entropy functional is defined as

$$F = -\sum_{i=1}^{N} f_i \ln(f_i) \tag{3.2}$$

Subject to the constraints

$$\alpha_i = \sum_{i=1}^{N} w_{i,i} f_i \qquad i = 1,\dots\dots\dots, M \quad \text{(projection data)} \tag{3.3}$$

and

$$f_i \geq 0 \qquad \text{(a prior condition)}$$

The Lagrangian multiplier technique has been used for maximization of the functional F under imposed constraints. The problem now reduced to the solution of a set of non-linear equations with unknown Lagrangian multipliers. Non-linear equations are solved after linearization using Taylor series expansion method, by Gauss-Seidel iterative technique (APPENDIX A) [45]

3.3.2 Minimum energy method

When a system is having minimum energy, then system is in most stable state. Based on the above definition formulations for minimum energy method is done as follows [31].

Minimum energy functional is defined as

$$F = -\sum_{j=1}^{N} f_j^{\,2} \qquad (3.4)$$

Subject to the constraints

$$\ddot{\alpha}_i = \sum_{j=1}^{N} w_{i,j} f_j \qquad i = 1,........M \qquad \text{(projection data)} \qquad (3.5)$$

The Lagrangian multiplier technique has been used for minimization of the functional F under imposed constraints. Problem reduced to the solution of a set of linear equations with Lagrangian multipliers unknown. Standard Gauss-Seidel method is used to solve the linear equations in Lagrangian multipliers and then filed values have been calculated (APPENDIX A) [45].

Chapter 4

Simulated Results and discussions on tomographic methods

The performance of the aforesaid discussed algorithms has been checked over simulated data. Mainly three field functions have been used to test performance constant, step, and impulse inside a unit circle. 61 rays and 12 views in 180° total view angle have generated projection data. Ray spacing during reconstructions has been taken 0.01639. During all reconstructions the initial values in the pixels inside the circle are taken 1.0 and outside forced to zero for the purpose of the application of the above discussed algorithms on a vertical pipe consisting of two-phase liquid metal flows.

4.1 Reconstruction errors

During the present work, five error norms have been reported.

$$E_A = \sqrt{\frac{\sum_{i=1}^{N}\left(f_i^{original} - f_i^{reconstructed}\right)^2}{N}} \qquad \text{RMS error} \qquad (4.1)$$

$$E_B = \sqrt{\frac{\sum_{i=1}^{N}\left(f_i^{original} - f_i^{reconstructed}\right)^2}{\sum_{i=1}^{N}\left(f_i^{original} - \tilde{f}\right)^2}} \qquad \text{normalized RMS error} \qquad (4.2)$$

$\tilde{f}$ is the original area average value of the field.

$$E_C = Max\left(\left|f_i^{original} - f_i^{reconstructed}\right|\right) \qquad \text{maximum absolute difference} \qquad (4.3)$$

$$E_D = \frac{\sum_{i=1}^{N}\left|f_i^{original} - f_i^{reconstructed}\right|}{N} \qquad \text{average error} \qquad (4.4)$$

$$E_E = \frac{\sum_{i=1}^{N}\left|f_i^{original} - f_i^{reconstructed}\right|}{\sum_{i=1}^{N}\left|f_i^{original}\right|} \qquad \text{normalized absolute error} \qquad (4.5)$$

Where, $f^{original}$, is assumed field for simulated projections, and $f^{reconstructed}$ is reconstructed field using simulated projections.

Relaxation parameter in algebraic reconstruction techniques is analogous to the *filter functions* in transform methods [42]. Opting for an appropriate relaxation parameter for minimum error reconstructions, in other way the most suitable relaxation parameter to watch out maximum features, is very important. Relaxation parameter has to do nothing with the convergence and higher relaxation parameter may take longer time than small one. It was assumed that if RMS error is at its minimum in an image reconstruction then the reconstructed image is with maximum possible features with that particular algorithm. E_A (RMS error) is used to find out the relaxation parameter(λ), relaxation parameter thus selected is corresponding to the minimum E_A (RMS error). Fig-(4.1)-(4.8) shows the variation of RMS error with relaxation parameter in step field reconstructions.
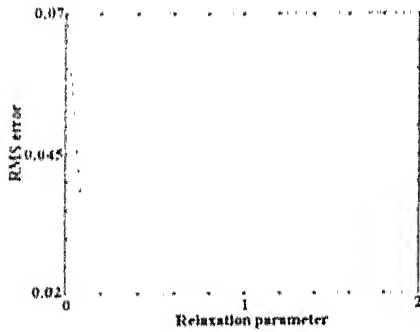
Fig-4.1 RMS error vs. relaxation parameter
for Simple ART for step field reconstruction
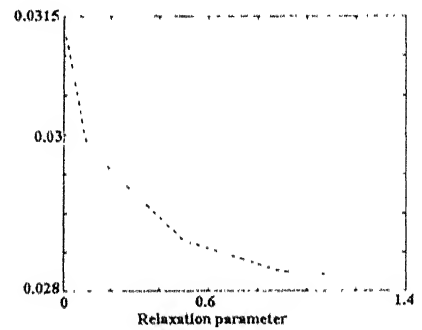
Fig-4.2 RMS error vs. relaxation parameter
for Anderson ART for step field reconstruction
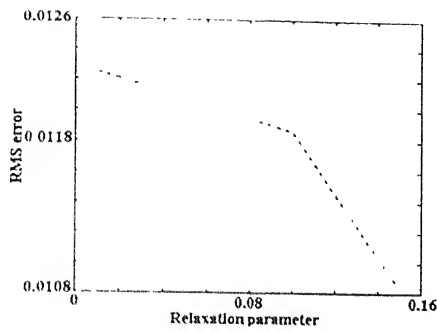
Fig-4.3 RMS error vs. relaxation parameter
for Gilbert ART for step field reconstruction
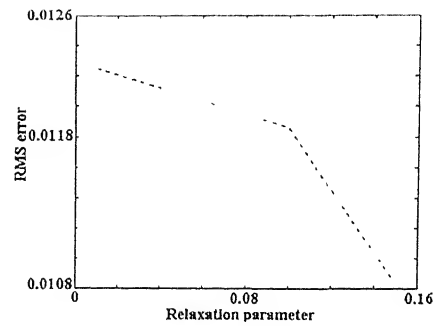
Fig-4.4 RMS error vs. relaxation parameter
for Gordon ART for step field reconstruction
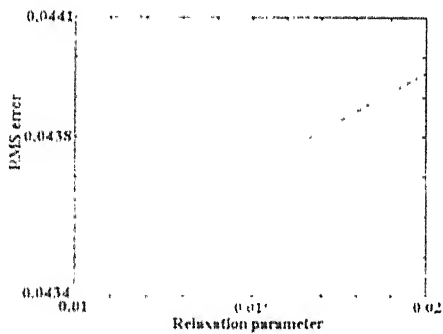
Fig-4.5 RMS error vs. relaxation parameter
for GBH MART for step field reconstruction
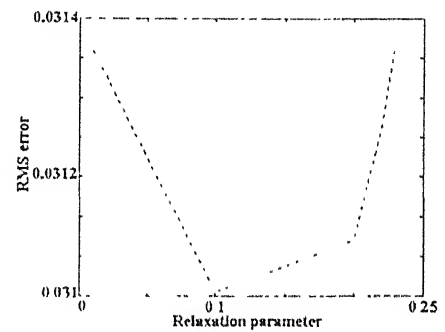
Fig-4.6 RMS error vs. relaxation parameter
for GH MART for step field reconstruction
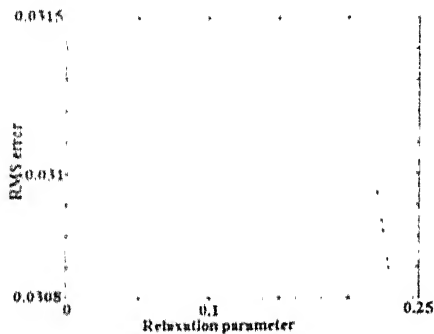
Fig-4.7 RMS error vs. relaxation parameter
for Lent MART for step field reconstruction
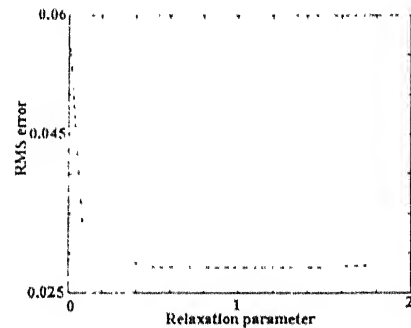
Fig-4.8 RMS error vs. relaxation parameter
for minimum energy for step field reconstruction

Fig-4.1 clearly shows that at the lower relaxation parameter in simple ART, RMS error is having steep change, later nearly a linear decrease. This trend also suggests that simple ART favors maximum and fastest features in an image reconstruction. Fig-4.2 does not

27

have any abrupt change in values, it rather gives nearly smooth change, and Anderson ART can reconstruct limited and slow features. Fig-4.3-4.4 again shows a smooth decrease, and suffers rather smaller range of relaxation parameter. Gilbert and Gordon ART cannot reconstruct the image with fast changing features, though it is desirable for better reconstruction. Fig-4.5-4.6 gives the profile of RMS error with relaxation parameter for GBH and GH MART respectively, having multiplicative corrections, and can reconstruct limited and slow features because higher relaxation parameter is not favorable. Fig-4.7 demonstrates the performance of Lent MART, preferring slow changes as of GH MART; error level is also small in this algorithm and most preferred among all MART algorithms. Fig-4.8 shows RMS error variation with relaxation parameter, and minimum energy method is found producing fast and maximum possible features in reconstruction and error level in this algorithm is also at minimum. The field values in the present step reconstruction, does not have fluctuating changes, and better image can be reconstructed with fast changing features (i.e. highest possible relaxation parameter). Table-4.1-4.21 demonstrates five errors in simulated constant, step and impulse field reconstructions.

Constant field						
λ	E_A	E_B	E_C	E_D	E_E	Iterations
0.01	3.450E-02	1.331E-02	7.118E-02	3.032E-02	6.064E-02	184
0.1	1.347E-02	5.197E-02	4.270E-02	1.090E-02	2.181E-02	81
0.5	1.180E-02	4.554E-02	4.493E-02	9.421E-03	1.884E-02	38
0.9	9.548E-03	3.684E-02	3.983E-02	7.638E-03	1.527E-02	273
1.3	8.?E-03	3.231E-02	3.583E-02	6.728E-03	1.345E-02	344
1.8	7.655E-03	2.953E-02	3.242E-02	6.195E-03	1.239E-02	349
1.9	7.560E-03	2.917E-02	3.187E-02	6.124E-03	1.224E-02	345

Table-4.1 Different error levels, number of iterations, and relaxation parameter are given for Simple ART constant function reconstructions

Constant field						
λ	E_A	E_B	E_C	E_D	E_E	Iterations
0.01	1.317E-02	5.085E-02	4.414E-02	1.050E-02	2.100E-02	81
0.1	9.953E-03	3.840E-02	4.111E-02	7.960E-03	1.592E-02	253
0.5	6.349E-03	2.449E-02	2.281E-02	5.225E-03	1.045E-02	239
0.9	1.852E-03	7.148E-03	5.521E-03	1.514E-03	3.028E-03	145
1.2	2.967E-03	1.145E-02	1.091E-02	2.445E-03	4.890E-03	303

Table-4.2 Different error levels, number of iterations, and relaxation parameter are given for Anderson ART constant function reconstructions

Constant field						
λ	E_A	E_B	E_C	E_D	E_E	Iterations
0.01	1.225E-02	4.729E-02	4.432E-02	9.712E-03	1.942E-02	195
0.1	1.186E-02	4.578E-02	4.398E-02	9.468E-03	1.893E-02	55
0.15	1.084E-02	4.185E-02	4.112E-02	8.663E-03	1.732E-02	126

Table-4.3 Different error levels, number of iterations, and relaxation parameter are given for Gilbert and Gordon ART constant function reconstructions

Constant field						
λ	E_A	E_B	E_C	E_D	E_E	Iterations
0.01	2.967E-02	1.145E-01	8.506E-02	2.363E-02	4.726E-02	355
0.02	3.161E-02	1.219E-01	9.171E-02	2.502E-02	5.004E-02	530

Table-4.4 Different error levels, number of iterations, and relaxation parameter are given for GBH MART constant function reconstructions

			Constant field			
λ	E_A	E_B	E_C	E_D	E_E	Iterations
0.01	8.677E-03	3.348E-02	3.080E-02	6.942E-03	1.388E-02	264
0.1	8.527E-03	3.290E-02	3.199E-02	6.788E-03	1.357E-02	58
0.2	9.100E-03	3.511E-02	3.451E-02	7.240E-03	1.448E-02	49
0.22	9.934E-03	3.833E-02	3.788E-02	7.902E-03	1.580E-02	73
0.23	1.110E-03	4.285E-02	4.287E-02	8.831E-03	1.766E-02	196

Table-4.5 Different error levels, number of iterations, and relaxation parameter are given for GH MART constant function reconstructions

			Constant field			
λ	E_A	E_B	E_C	E_D	E_E	Iterations
0.01	8.660E-03	3.341E-02	3.075E-02	6.929E-03	1.385E-02	258
0.1	8.310E-03	3.206E-02	3.115E-02	6.616E-03	1.323E-02	57
0.2	8.173E-03	3.153E-02	3.092E-02	6.511E-03	1.302E-02	44
0.22	7.872E-03	3.037E-02	3.009E-02	6.275E-03	1.255E-02	76
0.23	6.924E-03	2.671E-02	2.723E-02	5.528E-03	1.105E-02	212

Table-4.6 Different error levels, number of iterations, and relaxation parameter are given for Lent MART constant function reconstructions

			Constant field			
λ	E_A	E_B	E_C	E_D	E_E	Iterations
0.01	1.795E-02	6.928E-02	7.785E-02	1.425E-02	2.850E-02	61
0.1	8.081E-03	3.118E-02	3.487E-02	6.551E-03	1.310E-02	905
0.5	1.277E-02	4.930E-02	4.074E-02	1.015E-02	2.030E-02	174
0.8	1.087E-02	4.198E-02	4.049E-02	8.540E-03	1.709E-02	158
0.9	4.172E-03	1.610E-02	1.545E-02	3.397E-03	6.795E-03	963
1.3	4.097E-03	1.581E-02	2.570E-02	3.226E-03	6.453E-03	1459
1.5	3.910E-03	1.508E-02	4.031E-02	2.940E-03	5.880E-03	2017
1.8	4.902E-03	1.891E-02	8.870E-02	2.439E-03	4.879E-03	7659

Table-4.7 Different error levels, number of iterations, and relaxation parameter are given for minimum energy constant function reconstructions

	Step field					
λ	E_A	E_B	E_C	E_D	E_E	Iterations
0.01	6.981E-02	1.755E-01	2.017E-01	4.976E-02	6.863E-02	206
0.1	3.098E-02	7.791E-02	1.382E-01	1.937E-02	2.672E-02	183
0.5	2.995E-02	7.534E-02	1.377E-01	1.944E-02	2.682E-02	79
0.9	2.985E-02	7.509E-02	1.377E-01	1.947E-02	2.686E-02	54
1.3	2.978E-02	7.491E-02	1.376E-01	1.947E-02	2.686E-02	44
1.8	2.943E-02	7.403E-02	1.346E-01	1.929E-02	2.661E-02	97
1.9	2.938E-02	7.389E-02	1.341E-01	1.926E-02	2.657E-02	104

Table-4.8 Different error levels, number of iterations, and relaxation parameter are given for Simple ART step function reconstructions

	Step field					
λ	E_A	E_B	E_C	E_D	E_E	Iterations
0.01	3.125E-02	7.860E-02	1.405E-01	1.944E-02	2.681E-02	197
0.1	2.985E-02	7.509E-02	1.376E-01	1.948E-02	2.687E-02	57
0.5	2.865E-02	7.206E-02	1.228E-01	1.891E-02	2.609E-02	205
0.9	2.825E-02	7.105E-02	1.154E-01	1.858E-02	2.562E-02	254
1.1	2.822E-02	7.098E-02	1.151E-01	1.859E-02	2.564E-02	294

Table-4.9 Different error levels, number of iterations, and relaxation parameter are given for Anderson ART step function reconstructions

	Step field					
λ	E_A	E_B	E_C	E_D	E_E	Iterations
0.01	3.015E-02	7.583E-02	1.382E-01	1.938E-02	2.674E-02	354
0.1	2.987E-02	7.513E-02	1.362E-01	1.959E-02	2.702E-02	82
0.15	2.965E-02	7.458E-02	1.342E-01	1.946E-02	2.684E-02	118

Table-4.10 Different error levels, number of iterations, and relaxation parameter are given for Gilbert and Gordon ART step function reconstructions

Step field						
λ	E_A	E_B	E_C	E_D	E_E	Iterations
0.01	4.347E-02	1.093E-01	2.000E-01	3.341E-02	4.608E-02	413
0.02	4.396E-02	1.105E-01	2.032E-01	3.388E-02	4.673E-02	291

Table-4.11 Different error levels, number of iterations, and relaxation parameter are given for GBH MART step function reconstructions

Step field						
λ	E_A	E_B	E_C	E_D	E_E	Iterations
0.01	3.136E-02	7.888E-02	1.407E-01	2.025E-02	2.793E-02	505
0.1	3.105E-02	7.810E-02	1.405E-01	2.061E-02	2.843E-02	109
0.2	3.112E-02	7.827E-02	1.408E-01	2.070E-02	2.865E-02	68
0.22	3.126E-02	1.863E-02	1.416E-01	2.097E-02	2.892E-02	70
0.23	3.137E-02	1.890E-02	1.408E-01	2.123E-02	2.928E-02	188

Table-4.12 Different error levels, number of iterations, and relaxation parameter are given for GH MART step function reconstructions

Step field						
λ	E_A	E_B	E_C	E_D	E_E	Iterations
0.01	3.136E-02	7.888E-02	1.405E-01	2.024E-02	2.792E-02	503
0.1	3.102E-02	7.802E-02	1.403E-01	2.058E-02	2.839E-02	109
0.22	3.096E-02	7.787E-02	1.398E-01	2.061E-02	2.843E-02	72
0.23	3.066E-02	1.711E-02	1.366E-01	2.045E-02	2.820E-02	198

Table-4.13 Different error levels, number of iterations, and relaxation parameter are given for Lent MART step function reconstructions

			Step field			
λ	E_A	E_B	E_C	E_D	E_E	Iterations
0.01	5.587E-02	1.405E-01	1.731E-01	4.351E-02	6.001E-02	43
0.1	3.021E-02	7.599E-02	1.306E-01	2.064E-02	2.847E-02	1289
0.5	2.822E-02	7.098E-02	1.146E-01	1.861E-02	2.567E-02	2361
0.8	2.817E-02	7.085E-02	1.147E-01	1.863E-02	2.569E-02	2407
1.0	2.817E-02	7.086E-02	1.150E-01	1.865E-02	2.573E-02	2440
1.3	2.820E-02	7.090E-02	1.152E-01	1.868E-02	2.577E-02	2929
1.5	2.824E-02	7.104E-02	1.159E-01	1.873E-02	2.583E-02	4106
1.8	2.850E-02	7.169E-02	1.176E-01	1.905E-02	2.620E-02	5044
1.9	2.863E-02	7.201E-02	1.209E-01	1.898E-02	2.618E-02	12008

Table-4.14 Different error levels, number of iterations, and relaxation parameter are given for minimum energy step function reconstructions

			Impulse field			
λ	E_A	E_B	E_C	E_D	E_E	Iterations
0.01	1.349E-01	1.038E-01	6.900E-01	1.163E-01	4.646E-02	167
0.1	5.105E-02	3.930E-02	3.952E-01	3.619E-02	1.445E-02	97
0.5	4.562E-02	3.512E-02	3.022E-01	3.355E-02	1.339E-02	46
0.9	4.258E-02	3.278E-02	2.674E-01	3.140E-02	1.253E-02	125
1.3	4.008E-02	3.085E-02	2.662E-01	2.905E-02	1.160E-02	181
1.8	3.792E-02	2.919E-02	2.647E-01	2.717E-02	1.084E-02	220
1.9	3.763E-02	2.897E-02	2.645E-01	2.692E-02	1.075E-02	222

Table-4.15 Different error levels, number of iterations, and relaxation parameter are given for Simple ART impulse function reconstructions.

			Impulse field			
λ	E_A	E_B	E_C	E_D	E_E	Iterations
0.01	5.099E-02	3.925E-02	3.990E-01	3.584E-02	1.431E-02	100
0.1	4.343E-02	3.343E-02	2.068E-01	3.218E-02	1.284E-02	108
0.5	3.458E-02	2.662E-02	2.605E-01	2.425E-02	9.685E-03	184
0.9	2.827E-02	2.176E-02	2.222E-01	1.752E-02	6.996E-03	113
1.1	2.878E-02	2.215E-02	2.271E-01	1.792E-02	7.158E-03	27

Impulse field						
λ	E_A	E_B	E_C	E_D	E_E	Iterations
0.01	4.644E-02	3.575E-02	2.950E-01	3.456E-02	1.380E-02	308
0.1	4.550E-02	3.503E-02	2.717E-01	3.403E-02	1.359E-02	65
0.15	4.357E-02	3.354E-02	2.684E-01	3.229E-02	1.289E-02	114

Table-4.17 Different error levels, number of iterations, and relaxation parameter are given for Gilbert and Gordon ART impulse function reconstructions

Impulse field						
λ	E_A	E_B	E_C	E_D	E_E	Iterations
0.01	2.038E-01	1.569E-01	6.616E-01	1.605E-01	6.408E-02	392
0.02	2.234E-01	1.700E-01	7.200E-01	1.850E-01	6.704E-02	560

Table-4.18 Different error levels, number of iterations, and relaxation parameter are given for GBH MART impulse function reconstructions

Impulse field						
λ	E_A	E_B	E_C	E_D	E_E	Iterations
0.01	6.205E-02	4.770E-02	3.353E-01	4.794E-02	1.914E-02	404
0.1	5.448E-02	4.193E-02	2.897E-01	4.198E-02	1.676E-02	84
0.2	3.641E-02	2.803E-02	2.220E-01	2.652E-02	1.059E-02	48
0.22	3.401E-02	2.618E-02	2.037E-01	2.433E-02	9.715E-03	52
0.23	3.292E-02	2.534E-02	2.102E-01	2.328E-02	9.297E-03	115

Table-4.19 Different error levels, number of iterations, and relaxation parameter are given for GH MART impulse function reconstructions

	Impulse field					
λ	E_A	E_B	E_C	E_D	E_E	Iterations
0.01	6.227E-02	4.794E-02	3.361E-01	4.813E-02	1.921E-02	415
0.1	5.105E-02	3.930E-02	3.952E-01	3.619E-02	1.445E-02	97
0.2	5.908E-02	4.548E-02	3.030E-01	4.570E-02	1.827E-02	78
0.22	5.843E-02	4.498E-02	3.026E-01	4.519E-02	1.804E-02	85
0.23	5.277E-02	4.060E-02	2.993E-01	4.025E-02	1.607E-02	232

Table-4.20 Different error levels, number of iterations, and relaxation parameter are given for Lent MART impulse function reconstructions

	Impulse field					
λ	E_A	E_B	E_C	E_D	E_E	Iterations
0.01	1.290E-01	9.936E-02	6.958E-01	1.026E-01	4.099E-02	27
0.1	4.547E-02	3.500E-02	2.865E-01	3.212E-02	1.367E-02	1540
0.5	3.215E-02	2.475E-02	2.432E-01	2.201E-02	8.789E-03	1040
0.8	2.750E-02	2.117E-02	2.160E-01	1.680E-02	6.711E-03	2074
1.0	2.810E-02	2.164E-02	2.208E-01	1.728E-02	6.901E-03	798
1.3	2.756E-02	2.120E-02	2.176E-01	1.682E-02	6.716E-03	3714
1.5	2.771E-02	2.133E-02	2.175E-01	1.692E-02	6.755E-03	4275
1.8	2.825E-02	2.174E-02	2.203E-01	1.735E-02	6.928E-03	9095
1.9	2.838E-02	2.184E-02	2.212E-01	1.780E-02	7.109E-03	14697

Table-4.21 Different error levels, number of iterations, and relaxation parameter are given for Minimum energy impulse function reconstructions

GH MART algorithm has been reconstructing constant fields with minimum error, but suffers smaller range of relaxation parameter (can give limited features on reconstruction). Anderson ART has spanned a greater range of relaxation parameter and given reconstructions with an error slightly more than GH MART. Error levels in Gilbert and Gordon ART are equal but more than Anderson and GH MART. Lent MART is again reconstructing constant fields with same range of relaxation parameter as GH MART but the error levels are higher. Simple ART possibly can have slow as well as fast changes during reconstructions (Spanning whole possible range of relaxation parameter).

GBH MART and Maximum entropy method are found to have reconstructions with maximum error.

Overall it can be said that GH MART is the best algorithm for constant fields followed by Lent MART, Minimum energy and Simple ART. Minimum energy method gives minimum error in step and impulse field reconstructions; whereas the error levels are high in GBH MART and Maximum entropy method.

Only one value of relaxation parameter is only used to reconstruct three fields using maximum entropy method. These algorithms are slow and reconstruction takes too long time. Table-(4.22-4.24) shows the various reconstruction errors in maximum entropy method for three fields, reconstruction errors are more than minimum energy method.

Constant field						
λ	E_A	E_B	E_C	E_D	E_E	Iterations
0.1	1.290E-01	9.936E-02	6.958E-01	1.026E-01	4.099E-02	11

Table-4.22 Different error levels, number of iterations, and relaxation parameter are given for maximum entropy constant function reconstruction

Step field						
λ	E_A	E_B	E_C	E_D	E_E	Iterations
0.1	3.798E-02	9.553E-02	1.541E-01	2.787E-02	3.844E-02	27

Table-4.23 Different error levels, number of iterations, and relaxation parameter are given for maximum entropy step function reconstruction

Impulse field						
λ	E_A	E_B	E_C	E_D	E_E	Iterations
0.1	1.185E-01	9.121E-02	4.499E-01	9.415E-02	3.759E-02	15

Table-4.24 Different error levels, number of iterations, and relaxation parameter are given for maximum entropy impulse function reconstruction

4.2 Simulated results

area average 0.5
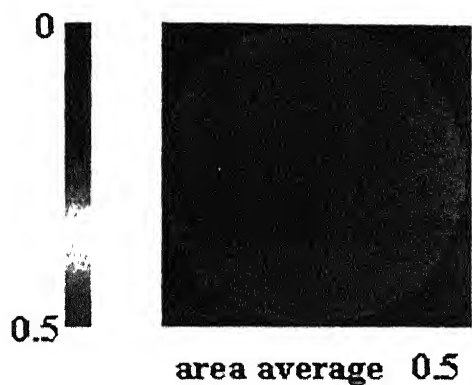
Fig-4.9 Constant original field

area average 0.5001
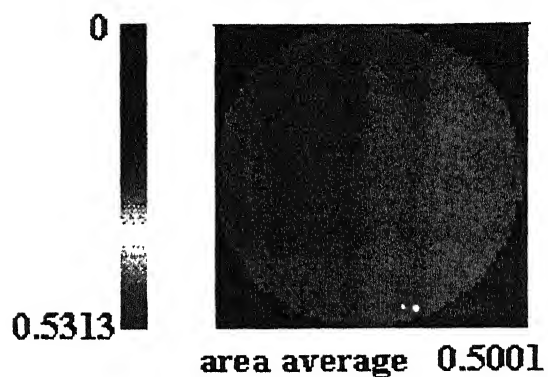
Fig-4.10 Reconstructed constant field
using Simple ART
(61 rays, 12 views, $\lambda = 1.99$)

area average 0.5000
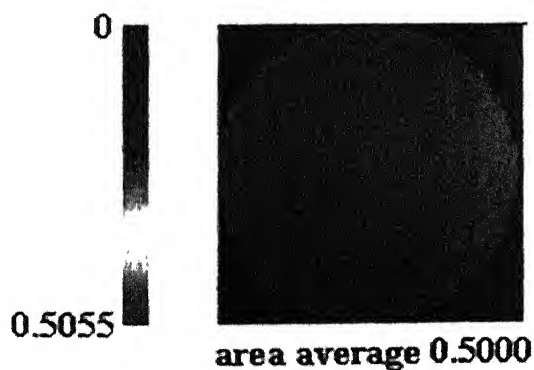
Fig-4.11 Reconstructed constant field
using Anderson ART
(61 rays, 12 views, $\lambda = 0.9$)

area average 0.5002
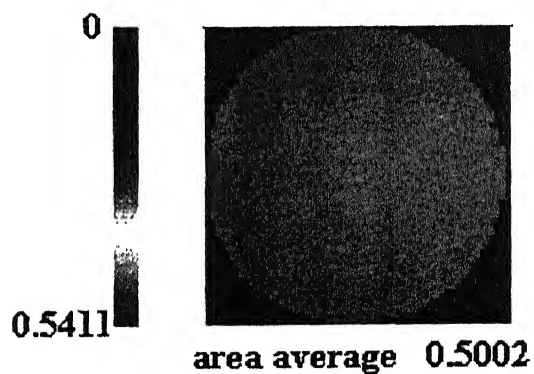
Fig-4.12 Reconstructed constant field
using Gilbert ART
(61 rays, 12 views, $\lambda = 0.15$)

0

0.5411

area average 0.5002
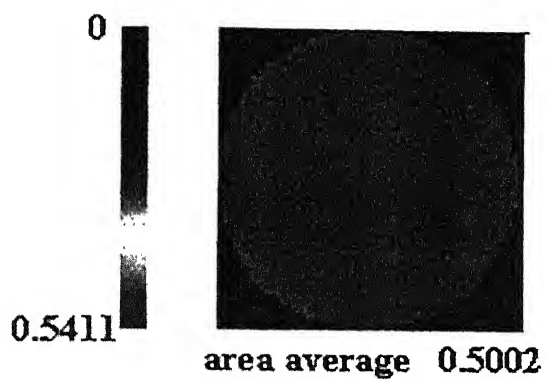
Fig-4.13 Reconstructed constant field

using Gordon ART

(61 rays, 12 views, $\lambda = 0.15$)

0

0.5789

area average 0.4992
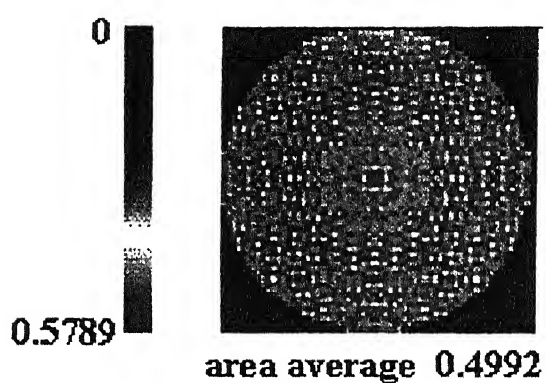
Fig-4.14 Reconstructed constant field

using GBH MART

(61 rays, 12 views, $\lambda = 0.01$)

0

0.5319

area average 0.5002
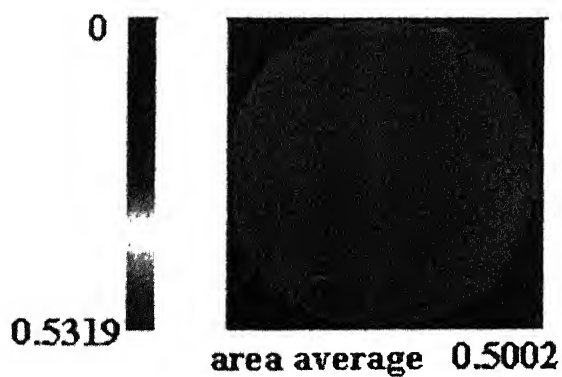
Fig-4.15 Reconstructed constant field

using GH MART

(61 rays, 12 views, $\lambda = 0.10$)

0

0.5300

area average 0.5001
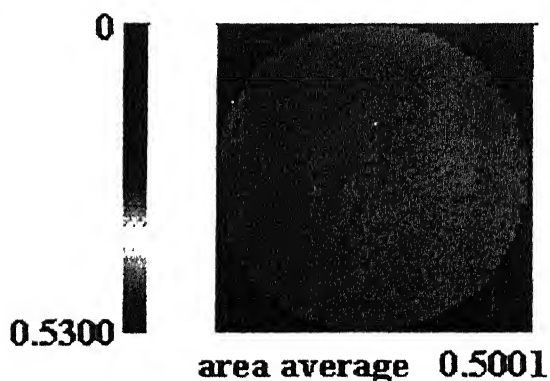
Fig-4.16 Reconstructed constant field

using Lent MART

(61 rays, 12 views, $\lambda = 0.22$)

area average 0.5001
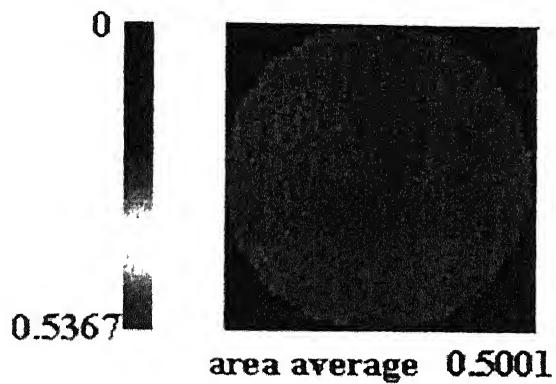
Fig-4.17 Reconstructed constant field
sing Maximum entropy method
(61 rays, 12 views, $\lambda = 0.1$)

area average 0.5002
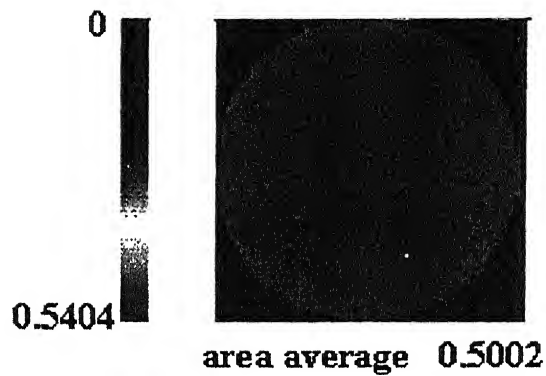
Fig-4.18 Reconstructed constant field
using Minimum energy method
(61 rays, 12 views, $\lambda = 0.8$)

area average 0.725
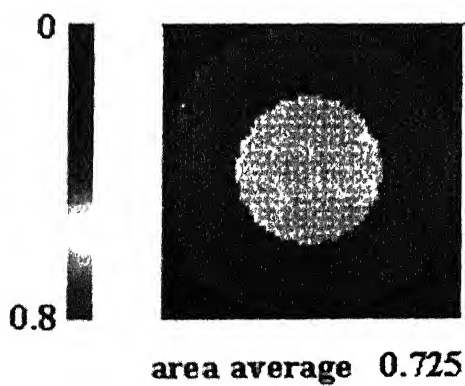
Fig-4.19 Step original field

area average 0.7251
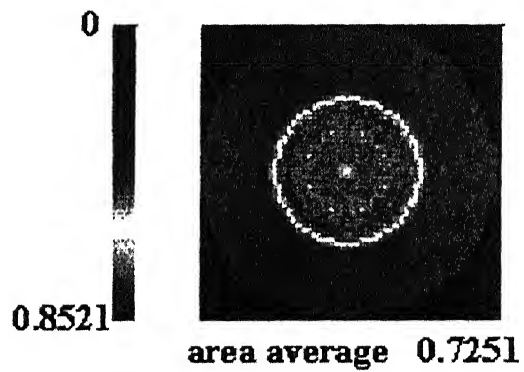
Fig-4.20 Reconstructed step field
using Simple ART
(61 rays, 12 views, $\lambda = 1.99$)

0

0.8460

area average   0.7250
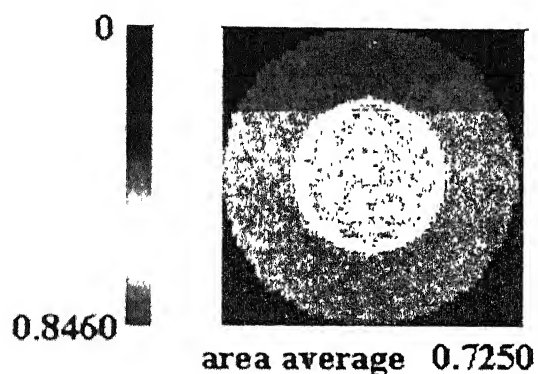
Fig-4.21 Reconstructed step field
using Anderson ART
(61 rays, 12 views, $\lambda = 0.9$)

0

0.8512

area average   0.7251
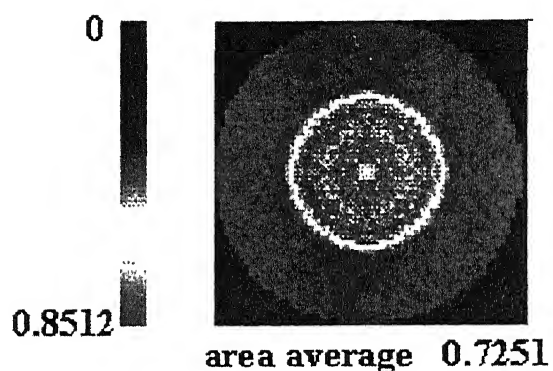
Fig-4.22 Reconstructed step field
using Gilbert ART
(61 rays, 12 views, $\lambda = 0.15$)

0

0.8512

area average   0.7251
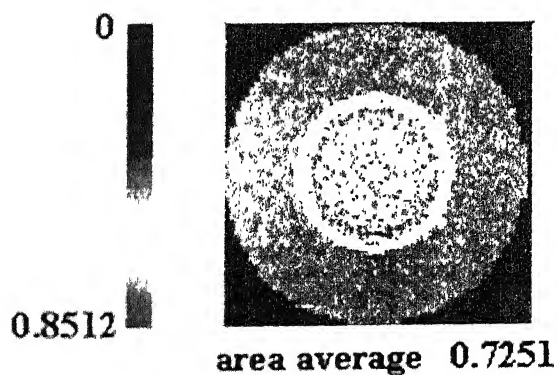
Fig- 4.23 Reconstructed step field
using Gordon ART
(61 rays, 12 views, $\lambda = 0.15$)

0

0.8507

area average   0.7252
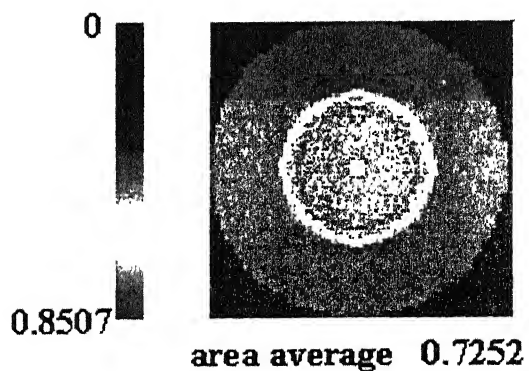
Fig-4.24 Reconstructed step field
using GBH MART
(61 rays, 12 views, $\lambda = 0.01$)

41

0

0.8587

area average 0.7251
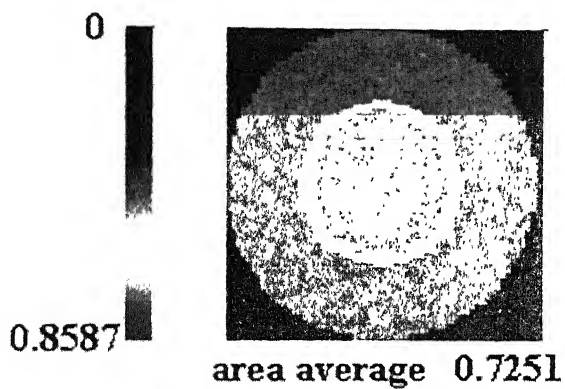
Fig-4.25 Reconstructed step field
using GH MART
(61 rays, 12 views, $\lambda = 0.1$)

0

0.8581

area average 0.7251
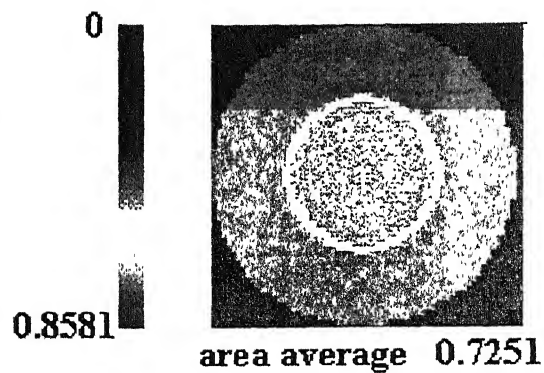
Fig-4.26 Reconstructed step field
using Lent MART
(61 rays, 12 views, $\lambda = 0.22$)

0

0.9063

area average 0.7248
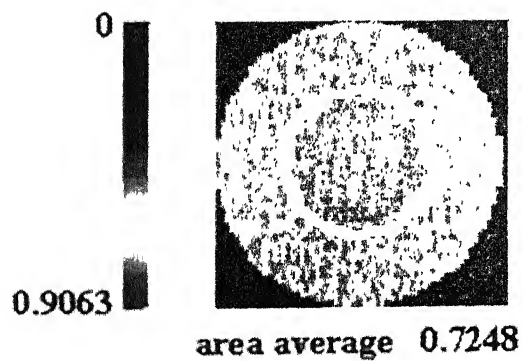
Fig-4.27 Reconstructed step field
using Maximum entropy
(61 rays, 12 views, $\lambda = 0.1$)

0

0.8436

area average 0.7250
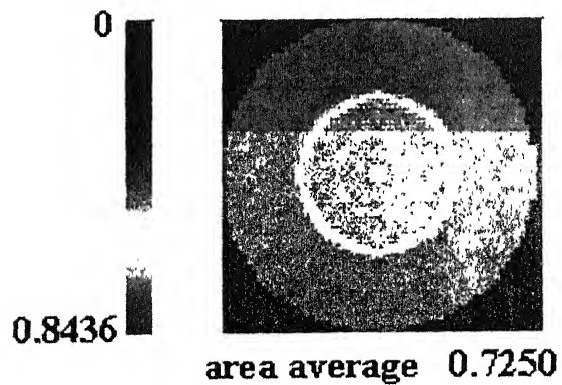
Fig-4.28 Reconstructed step field
using Minimum energy
(61 rays, 12 views, $\lambda = 0.8$)

42

0

3.1282

area average   2.5042
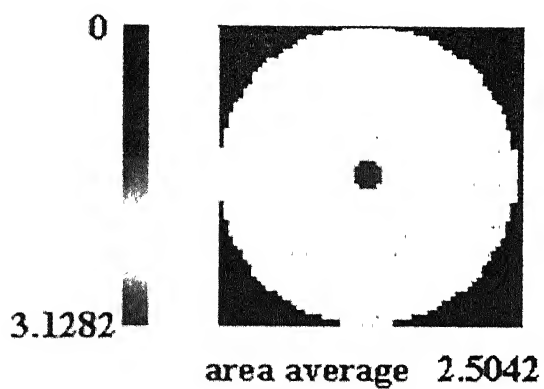
Fig-4.29 Impulse original field

0

3.1086

area average   2.5040
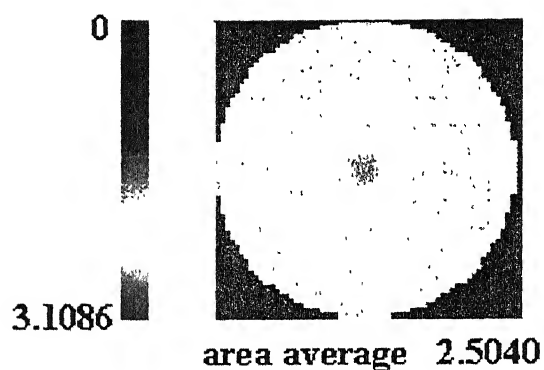
Fig-4.30 Reconstructed impulse field
using Simple ART
(61 rays, 12 views, $\lambda = 1.99$)

0

3.1075

area average   2.5044
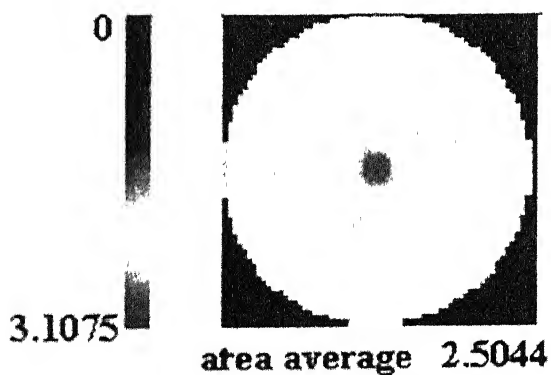
Fig-4.31 Reconstructed impulse field
using Anderson ART
(61 rays, 12 views, $\lambda = 0.9$)

0

3.0932

area average   2.5037
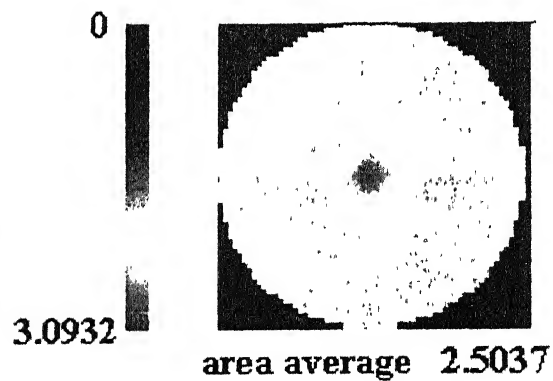
Fig-4.32 Reconstructed impulse field
using Gilbert ART
(61 rays, 12 views, $\lambda = 0.15$)

0

3.0932

area average 2.5037
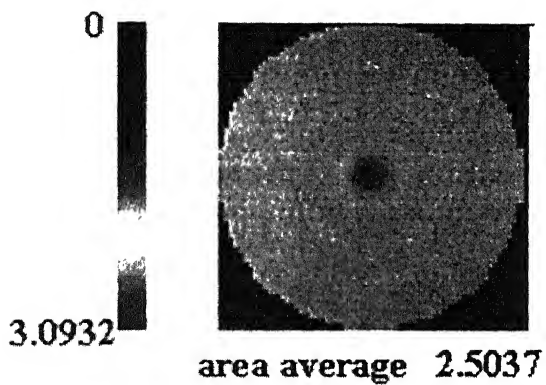
Fig-4.33 Reconstructed impulse field
using Gordon ART
(61 rays, 12 views, $\lambda = 0.15$)

0

3.5530

area average 2.5092
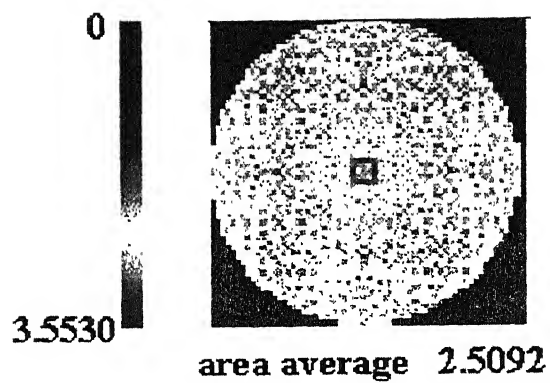
Fig-4.34 Reconstructed impulse field
using GBH MART
(61 rays, 12 views, $\lambda = 0.01$)

0

3.0872

area average 2.5033
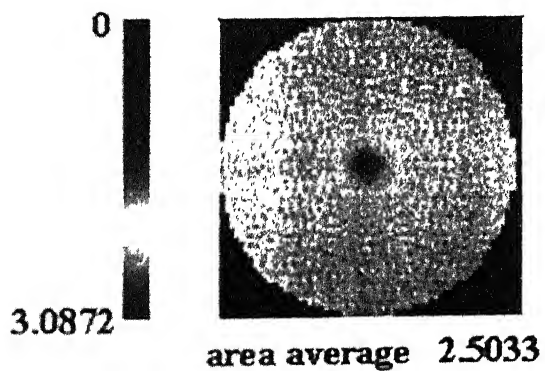
Fig-4.35 Reconstructed impulse field
using GH MART
(61 rays, 12 views, $\lambda = 0.1$)

0

3.1042

area average 2.5032
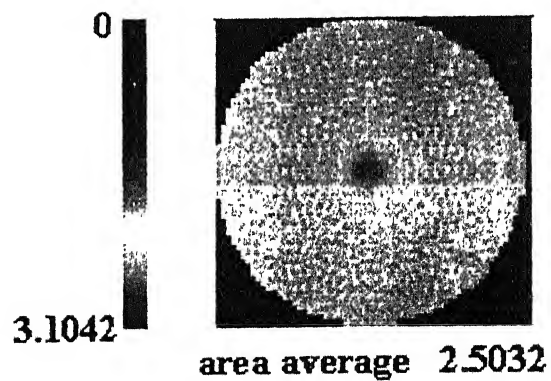
Fig-4.36 Reconstructed impulse field
using Lent MART
(61 rays, 12 views, $\lambda = 0.22$)

44

0

3.0391

area average 2.5012
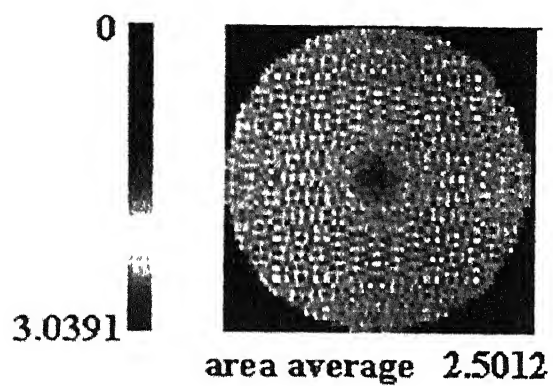
Fig–4.37 Reconstructed impulse field

using Maximum entropy

61 rays, 12 views, $\lambda = 0.1$)

0

3.1080

area average 2.5044
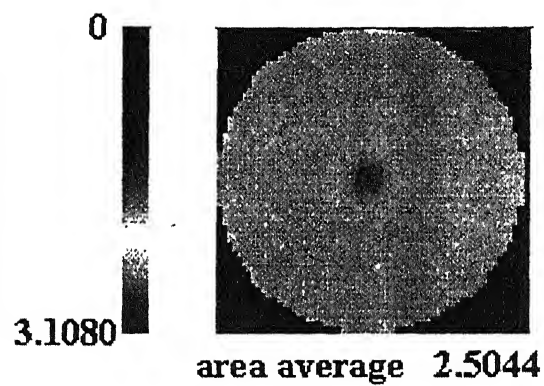
Fig-4.38 Reconstructed impulse field

using Minimum energy

(61 rays, 12 views, $\lambda = 0.8$)

4.3 Discussions over simulated results

All the mentioned algorithms have been extensively studied for the range of relaxation parameter and five aforementioned error norms for constant, step, and impulse reconstructions. First two of the Above-mentioned reconstructed fields, can be used to construct any function, in addition the third function, which is studied in the present work, is impulse. The basic purpose of considering this function in the present study is to see the sensitivity of these algorithms towards a pulse change in the field.

As earlier mentioned, relaxation parameter acts as a *filter function*, means if relaxation parameter is small it signifies slow changes during reconstruction. A study of relaxation parameter with RMS error with step function reconstructions is presented. It can be seen easily in the given Fig-(4.1-4.8) that RMS error is minimum for fast changes, moreover it depends upon the type of field one want to reconstruct., except in GBH MART, GH MART, and Minimum energy method, where medium changes are preferred. Anderson ART and Simple ART have almost covered the whole possible range of relaxation parameter. Simple ART always shows a convergence whereas Anderson ART starts showing diverging characteristics as relaxation parameter goes beyond 1.1, and after this it is at the verge of divergence. Gilbert ART and Gordon ART can be used up to relaxation parameter 0.15, beyond which they show divergence characteristics (i.e. not able to show the features corresponding to higher relaxation). GBH MART shows convergence up to 0.02 however this range goes a little above for both GH and LENT MART (up to 0.22).

All the algorithms are highly sensitive to the initial guess, especially multiplicative ART methods. Initial guess can entirely change the error norms and their distributions for large relaxation parameters and may also lead to divergence.

At last, it can be concluded that Anderson ART, GH MART, Lent MART and Minimum energy methods are the best algorithms for low error reconstructions. Simple ART and Anderson ART are good enough (can reconstruct maximum features of an image) for large range of relaxation parameter. GBH MART and Maximum Entropy method have shown larger error in reconstruction.

Chapter 5

Two-fluid model for void fraction patterns in liquid metal two-phase flows

The accurate prediction of two-phase flow dynamics with respect to the boiling and condensation conditions is essential for the safety of nuclear reactors. However for gas driven ADS systems two-phase flow studies, without interfacial mass transport are required [10].

Transient two-dimensional two-fluid model has been used to address the development of gas-driven ADS systems. This model considers each phase separately expressed in terms of two sets of conservation equations governing the balance of mass, momentum and energy in each phase. They are complemented by the set of interfacial jump conditions (balance over discontinuities) with proper assumptions. Various suitable constitutive relations have been utilized [2, 8].

5.1 Model formulation and assumptions

Model formulation is now being discussed in detail [2, 8]. This is a six-equation model, considering each phase separately. Continuity equation has been written for both the phases separately with "smear densities" (the product of density and volume fraction). Interfacial mass transfer is absent in the present case (there is no phase change). Momentum equations are coupled with microscopic viscous momentum transfer, pressure equilibrium and interfacial momentum transfer. To simulate interfacial momentum transfer between two-phases in direct contact, a term "Momentum Transfer Coefficient (K)" has been considered and it is assumed that momentum transfer between the two-phases is proportional to the velocity difference between two-phases [2, 4]. Coupling interfacial drag in this way has an advantage that it gives linearized implicit coupling between fields and K itself can vary with velocity [4].

$$\text{Generalized interfacial drag} = K\left|\left(\underline{U_l} - \underline{U_g}\right)\right|$$

K incorporates steady and transient forces, in steady forces only skin drag has been considered as turbulence has been neglected. On the other hand transient forces can be

fragmented in two parts, virtual mass force and Basset force. Virtual mass force is the force caused by the virtual mass around the bubble. Basset force is caused by the acceleration of boundary layer around the bubble. Faxen force has been neglected from our analysis because of its unimportance in bubbly, slug and churn turbulent flows. This needs special attention only in separated flows [12].

Certain elements of complex microphysics of exchange processes, such as the effect of momentum mixing (turbulence), have been neglected. Thus form drag has also been dropped out of steady drag formulations; moreover its associated energy dissipation and detailed distinction of interfacial properties from the bulk properties are also neglected. The effect of drag dissipation has been assigned completely to the heating of vapor [4].

Interfacial forced convection heat transfer term, again for linear implicitness in numerical procedure, is written as [4],

$$\text{Interfacial forced convection term} = R\left|(T_l - T_g)\right|$$

The equations are also having microscopic viscous dissipation and microscopic conduction heat transfer within single phase [2, 4, and 8]. Turbulent heat flux and interfacial viscous heat dissipation (Faxen work) have been neglected [12]. Due to the absence of interfacial mass transport only two jump conditions are required to handle interfacial discontinuities. Firstly the sum total of interfacial momentum is equal to zero and secondly, net interfacial heat transfer is equal to zero [8].

First jump condition gives rise to an assumption, which is the equality of mean pressures of the two phases (i.e. $P_l = P_g$) [2, 4, and 8]. However this is not a very good assumption, since with this assumption pressure waves travel with same speed in both the phases, i.e. gas and liquid. The isentropic acoustic velocities of liquid and gas differ a lot. This assumption has been frequently used earlier and hence has been utilized here too [17]. Second jump condition for interfacial heat transport is handled considering zero entropy production at interfaces with infinitely small interfacial thickness; implementation needs a higher value of R and leads to the equality of gas and liquid temperatures [2, 4].

5.2 Conservation equations

Continuity equations

$$\frac{\partial \rho_g^{'}}{\partial t} + \underline{\nabla} \bullet \left(\rho_g^{'} \underline{U}_g\right) = 0 \qquad (5.1)$$

$$\frac{\partial \rho_l^{'}}{\partial t} + \underline{\nabla} \bullet \left(\rho_l^{'} \underline{U}_l\right) = 0 \qquad (5.2)$$

Momentum equations

$$\frac{\partial \left(\rho_g^{'} \underline{U}_g\right)}{\partial t} + \underline{\nabla} \bullet \left(\rho_g^{'} \underline{U}_g \underline{U}_g\right) = -\alpha \underline{\nabla} P + K\left(\underline{U}_l - \underline{U}_g\right) + \underline{\nabla} \bullet \left(\alpha \underline{\sigma}_g\right) \qquad (5.3)$$

$$\frac{\partial \left(\rho_l^{'} \underline{U}_l\right)}{\partial t} + \underline{\nabla} \bullet \left(\rho_l^{'} \underline{U}_l \underline{U}_l\right) = -(1-\alpha)\underline{\nabla} P + K\left(\underline{U}_g - \underline{U}_l\right) + \underline{\nabla} \bullet \left((1-\alpha)\underline{\sigma}_l\right) \qquad (5.4)$$

Note that the factors α and $1-\alpha$ (in equations 5.3 and 5.4) lie outside the pressure gradient. If these factors were within the gradient, as some authors have proposed, then the equations could not represent static equilibrium for an inhomogeneous distribution in the absence of gravity [4].

Energy equations

$$\frac{\partial \left(\rho_g^{'} I_g\right)}{\partial t} + \nabla \bullet \left(\rho_g^{'} I_g U_g\right) = -P\left(\frac{\partial \alpha}{\partial t} + \nabla \bullet \left(\alpha \underline{U}_g\right)\right) + K\left(\underline{U}_g - \underline{U}_l\right)^2 + R(T_l - T_g) + \alpha \underline{\sigma}_g \bullet \left(\underline{\nabla U}_g\right) + \underline{\nabla} \bullet K_g \alpha \underline{\nabla} T_g \qquad (5.5)$$

$$\frac{\partial \left(\rho_l^{'} I_l\right)}{\partial t} + \nabla \bullet \left(\rho_l^{'} I_l U_l\right) = -P\left(\frac{\partial (1-\alpha)}{\partial t} + \underline{\nabla} \bullet \left((1-\alpha)\underline{U}_l\right)\right) + R(T_g - T_l) + (1-\alpha)\underline{\sigma}_l \bullet \left(\underline{\nabla U}_l\right) + \underline{\nabla} \bullet K_l (1-\alpha)\underline{\nabla} T_l \qquad (5.6)$$

5.3 Constitutive equations

Few more equations are needed to complete this model. These equations are as follows.

$$\rho_g^{'} = \alpha \rho_g \qquad (5.7)$$

$$\rho_l^{'} = (1-\alpha)\rho_l \qquad (5.8)$$

Where, $\rho_l^{'}, \rho_g^{'}$ are macroscopic liquid and gas densities (mass per unit of mixture volume) and ρ_l, ρ_g are microscopic liquid and gas densities (mass of liquid per unit of liquid volume). Liquid is assumed incompressible and ideal equation of state for gas has been utilized.

Equation of state for gas

$$P = \frac{\rho_g R T_g}{m_w} \qquad (5.9)$$

For ideal gas under adiabatic reversible compression, i.e. isentropic process, acoustic velocity for gas is given as,

$$a_g^2 = \frac{dP}{d\rho} = \frac{dP}{dV} * \frac{dV}{d\rho} = (-\gamma \frac{P}{V}) * (-\frac{V^2}{m}) = \frac{\gamma}{m} PV = \frac{\gamma}{m} nRT = \gamma \frac{1}{mw} RT$$

$$a_g = \sqrt{\gamma RT / m_w} = \sqrt{\gamma P / \rho} \qquad (5.10)$$

Where, m_w is the molecular weight of gas, and m is the mass of the gas.

The viscous stress tensors $\underline{\sigma}_l$ and $\underline{\sigma}_g$ are the usual Newtonian ones for liquid and gas respectively, in two-dimensional cylindrical coordinates, viscous stress tensors for liquid is being given and a similar set for gas holds [13].

$$(\sigma_{lrr}) = 2\mu_l \frac{\partial u_l}{\partial r} + \lambda_l \left(\frac{1}{r} \frac{\partial (ru_l)}{\partial r} + \frac{\partial v_l}{\partial z} \right) \qquad (5.11)$$

$$(\sigma_{lrz}) = \mu_l \left(\frac{\partial v_l}{\partial r} + \frac{\partial u_l}{\partial z} \right) \qquad (5.12)$$

$$(\sigma_{lzz}) = 2\mu_l \frac{\partial v_l}{\partial z} + \lambda_l \left(\frac{1}{r} \frac{\partial (ru_l)}{\partial r} + \frac{\partial v_L}{\partial z} \right) \qquad (5.13)$$

$$(\sigma_{l\Phi\Phi}) = 2\mu_l \frac{u_l}{r} + \lambda_l \left(\frac{1}{r} \frac{\partial (ru_l)}{\partial r} + \frac{\partial v_l}{\partial z} \right) \qquad (5.14)$$

μ_l is the liquid coefficient of viscosity (dynamic viscosity), and λ_l is the second coefficient of viscosity for liquids. The two coefficients of viscosity are related to the coefficient of bulk viscosity k by the expression [13],

$$k = \frac{2}{3} \mu_l + \lambda_l \qquad (5.15)$$

In general, it is believed that k is negligible except in the study of the structure of shock waves and in the absorption and attenuation of acoustic waves. For this reason, bulk viscosity k is ignored. With $k = 0$, the second coefficient of viscosity becomes,

50

$$\lambda_l = -\frac{2}{3}\mu_l \qquad\qquad (5.16)$$

Same expressions of second coefficient of viscosity have been utilized with gas also.

5.4 Numerical procedure

The basic numerical procedure is an extension of the Implicit, Continuous-fluid, Eulerian technique (ICE), which allows for fluid dynamic studies at all flow speeds [3]. Although the technique has been applied to generalized Eulerian-Lagrangian representations, the present multiphase flow version is restricted to a purely Eulerian mesh of computational cells. This technique is referred as an Implicit, Multi-Field (IMF) solution method [4]. Among its properties are the following [4],

1. Implicit treatment of mass convection and equation of state, so that flow speeds can range from far subsonic (incompressible) to supersonic.

2. Implicit coupling among the fields, to allow forces that range from very weak to those strong enough to completely tie the fields together.

The Eulerian mesh of finite-difference cells is used. In cylindrical coordinates these cells are toroids about the axis, rectangular in cross-section and with dimensions δr and δz whereas in Cartesian coordinates these cells are rectangular.
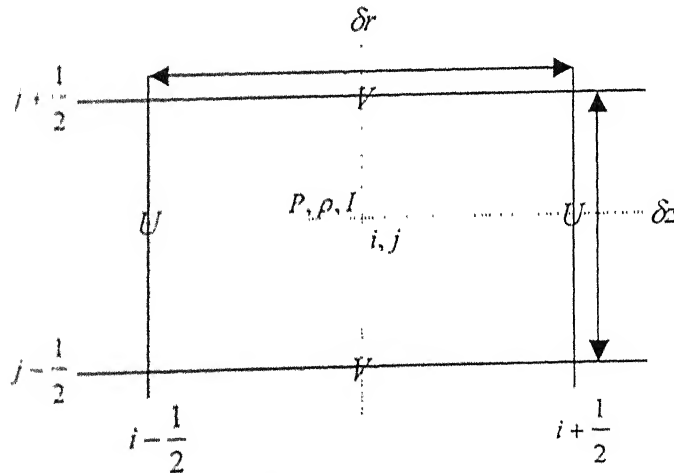
Fig-5.1 Layout of field variables and indices for a computational cell

5.4.1 Convective fluxes

There are various ways in which mass, energy, and momentum convective fluxes can be written, the precise form being irrelevant to the conceptual formulation of IMF technique, but nevertheless crucial to the assurance of accuracy and numerical stability of the calculations. Partial donor cell differencing has been utilized in this analysis, according to it [3]:

$$\left(\rho u^2\right)_{i,j} = \frac{\left(\rho_{i,j} + \rho_{i-1,j}\right)}{2} u_{i-\frac{1}{2},j} \frac{\left(u_{i-\frac{1}{2},j} + u_{i+\frac{1}{2},j}\right)}{2} \quad \text{for } \frac{\left(u_{i-\frac{1}{2},j} + u_{i+\frac{1}{2},j}\right)}{2} > 0$$

$$\left(\rho u^2\right)_{i,j} = \frac{\left(\rho_{i,j} + \rho_{i+1,j}\right)}{2} u_{i+\frac{1}{2},j} \frac{\left(u_{i-\frac{1}{2},j} + u_{i+\frac{1}{2},j}\right)}{2} \quad \text{for } \frac{\left(u_{i-\frac{1}{2},j} + u_{i+\frac{1}{2},j}\right)}{2} \leq 0 \quad (5.16)$$

$$\left(\rho u\right)_{i+\frac{1}{2},j} = \rho_{i,j} u_{i+\frac{1}{2},j} \quad \text{for } u_{i+\frac{1}{2},j} > 0$$

$$\left(\rho u\right)_{i+\frac{1}{2},j} = \rho_{i+1,j} u_{i+\frac{1}{2},j} \quad \text{for } u_{i+\frac{1}{2},j} \leq 0 \quad (5.17)$$

In the same way energy convection fluxes have been discretized. Partial donor cell flux is not space centered and has low order truncation errors. These contribute a positive diffusive effect and hence tend to automatically stabilize the numerical calculations.

5.4.2 Finite difference formulations

The finite difference formulations for all the equations have been presented below [4].

$$\left(\rho'_g\right)^{n+1}_{i,j} = \left(\rho'_g\right)^{n}_{i,j} - \delta t \left(\left(\rho'_g u_g r\right)^{n+1}_{i+\frac{1}{2},j} - \left(\rho'_g u_g r\right)^{n+1}_{i-\frac{1}{2},j}\right) / r_i \delta r$$
$$- \delta t \left(\left(\rho'_g v_g\right)^{n+1}_{i,j+\frac{1}{2}} - \left(\rho'_g v_g\right)^{n+1}_{i,j-\frac{1}{2}}\right) / \delta z \qquad (5.18)$$

$$\left(\rho'_g u_g\right)^{n+1}_{i+\frac{1}{2},j} = (G)_{i+\frac{1}{2},j} - \delta t \alpha^{n+1}_{i+\frac{1}{2},j} \left(p^{n+1}_{i+1,j} - p^{n+1}_{i,j}\right) / \delta r$$
$$+ \delta t K^n_{i+\frac{1}{2},j} \left((u_l)^{n+1}_{i+\frac{1}{2},j} - (u_g)^{n+1}_{i+\frac{1}{2},j}\right) \qquad (5.19)$$

$$(\rho_g v_g)^{n+1}_{i,j+\frac{1}{2}} = (G)_{i,j+\frac{1}{2}} - \delta t \, \alpha^{n+1}_{i,j+\frac{1}{2}}(p^{n+1}_{i,j+1} - p^{n+1}_{i,j})/\delta z$$

$$+ \delta t K^{n}_{i,j+\frac{1}{2}}[(v_l)^{n+1}_{i,j+\frac{1}{2}} - (v_g)^{n+1}_{i,j+\frac{1}{2}}] \tag{5.20}$$

$$(\rho_l)^{n+1}_{i,j} = (\rho_l)^{n}_{i,j} - \delta t \left((\rho_l u_l r)^{n+1}_{i+\frac{1}{2},j} - (\rho_l u_l r)^{n+1}_{i-\frac{1}{2},j}\right)/r_i \delta r$$

$$\delta t \left((\rho_l v_l)^{n+1}_{i,j+\frac{1}{2}} - (\rho_l v_l)^{n+1}_{i,j-\frac{1}{2}}\right)/\delta z \tag{5.21}$$

$$(\rho_l u_l)^{n+1}_{i+\frac{1}{2},j} = (L)_{i+\frac{1}{2},j} - \delta t \left(1 - \alpha^{n+1}_{i+\frac{1}{2},j}\right)\left(p^{n+1}_{i+1,j} - p^{n+1}_{i,j}\right)/\delta r$$

$$+ \delta t K^{n}_{i+\frac{1}{2},j}\left((u_g)^{n+1}_{i+\frac{1}{2},j} - (u_l)^{n+1}_{i+\frac{1}{2},j}\right) \tag{5.22}$$

$$(\rho_l v_l)^{n+1}_{i,j+\frac{1}{2}} = (L)_{i,j+\frac{1}{2}} - \delta t \left(1 - \alpha^{n+1}_{i,j+\frac{1}{2}}\right)\left(p^{n+1}_{i,j+1} - p^{n+1}_{i,j}\right)/\delta z$$

$$+ \delta t K^{n}_{i,j+\frac{1}{2}}[(v_g)^{n+1}_{i,j+\frac{1}{2}} - (v_l)^{n+1}_{i,j+\frac{1}{2}}] \tag{5.23}$$

Where, the quantities $(G)_{i+\frac{1}{2},j}, (G)_{i,j+\frac{1}{2}}$, $(L)_{i+\frac{1}{2},j}$, and $(L)_{i,j+\frac{1}{2}}$ account for the effects of momentum convection, gravity, and viscous stress. These have been used at time level n [4] making this technique semi-implicit.

$$(G)_{i+\frac{1}{2},j} = (\rho_g u_g)^{n}_{i+\frac{1}{2},j} - \delta t \left((\rho_g u_g^2 r)^{n}_{i+1,j} - (\rho_g u_g^2 r)^{n}_{i,j}\right)/r_{i+\frac{1}{2}} \delta r$$

$$- \delta t \left((\rho_g u_g v_g)^{n}_{i+\frac{1}{2},j+\frac{1}{2}} - (\rho_g u_g v_g)^{n}_{i+\frac{1}{2},j-\frac{1}{2}}\right)/\delta z$$

$$+ \delta t \left(r_{i+1}\alpha^{n}_{i+1,j}(\sigma_{grr})^{n}_{i+1,j} - r_i \alpha^{n}_{i,j}(\sigma_{grr})^{n}_{i,j}\right)/r_{i+\frac{1}{2}} \delta r$$

$$+ \delta t \left(\alpha^{n}_{i+\frac{1}{2},j+\frac{1}{2}}(\sigma_{grz})^{n}_{i+\frac{1}{2},j+\frac{1}{2}} - \alpha^{n}_{i+\frac{1}{2},j-\frac{1}{2}}(\sigma_{grz})^{n}_{i+\frac{1}{2},j-\frac{1}{2}}\right)/\delta z$$

$$- \delta t \alpha^{n}_{i+\frac{1}{2},j}(\sigma_{g\Phi\Phi})^{n}_{i+\frac{1}{2},j}/r_{i+\frac{1}{2}} \tag{5.24}$$

53

$$(G)_{i,j+\frac{1}{2}} = (\rho'_g v_g)^n_{i,j+\frac{1}{2}} - \delta t \left((\rho'_g u_g v_g r)^n_{i+\frac{1}{2},j+\frac{1}{2}} - (\rho'_g u_g v_g r)^n_{i-\frac{1}{2},j+\frac{1}{2}} \right) / r_i \delta r$$

$$\delta t \left((\rho'_g v^2_g)^n_{i,j+1} - (\rho'_g v^2_g)^n_{i,j} \right) / \delta z$$

$$+ \delta t (\rho'_g)^n_{i,j+\frac{1}{2}} g$$

$$+ \delta t \left(r_{i+\frac{1}{2}} \alpha^n_{i+\frac{1}{2},j+\frac{1}{2}} (\sigma_{grz})^n_{i+\frac{1}{2},j+\frac{1}{2}} - r_{i-\frac{1}{2}} \alpha^n_{i-\frac{1}{2},j+\frac{1}{2}} (\sigma_{grz})^n_{i-\frac{1}{2},j+\frac{1}{2}} \right) / r_i \delta r$$

$$+ \delta t \left(\alpha^n_{i,j+1} (\sigma_{gzz})^n_{i,j+1} - \alpha^n_{i,j} (\sigma_{gzz})^n_{i,j} \right) / \delta z \tag{5.25}$$

$$(I)_{i,j} = (\rho'_l u_l)^n_{i+\frac{1}{2},j} - \delta t \left((\rho'_l u^2_l r)^n_{i+1,j} - (\rho'_l u^2_l r)^n_{i,j} \right) / r_{i+\frac{1}{2}} \delta r$$

$$\delta t \left((\rho'_l u_l v_l)^n_{i+\frac{1}{2},j+\frac{1}{2}} - (\rho'_l u_l v_l)^n_{i+\frac{1}{2},j-\frac{1}{2}} \right) / \delta z$$

$$+ \delta t \left(r_{i+1} (1 - \alpha^n_{i+1,j}) (\sigma_{lrr})^n_{i+1,j} - r_i (1 - \alpha^n_{i,j}) (\sigma_{lrr})^n_{i,j} \right) / r_{i+\frac{1}{2}} \delta r$$

$$+ \delta t \left((1 - \alpha^n_{i+\frac{1}{2},j+\frac{1}{2}}) (\sigma_{lrz})^n_{i+\frac{1}{2},j+\frac{1}{2}} - (1 - \alpha^n_{i+\frac{1}{2},j-\frac{1}{2}}) (\sigma_{lrz})^n_{i+\frac{1}{2},j-\frac{1}{2}} \right) / \delta z$$

$$\delta t (1 - \alpha^n_{i+\frac{1}{2},j}) (\sigma_{l\theta\theta})^n_{i+\frac{1}{2},j} / r_{i+\frac{1}{2}} \tag{5.26}$$

$$(L)_{i,j} = (\rho'_l v_l)^n_{i,j+\frac{1}{2}} - \delta t \left((\rho'_l u_l v_l r)^n_{i+\frac{1}{2},j+\frac{1}{2}} - (\rho'_l u_l v_l r)^n_{i-\frac{1}{2},j+\frac{1}{2}} \right) / r_i \delta r$$

$$\delta t \left((\rho'_l v^2_l)^n_{i,j+1} - (\rho'_l v^2_l)^n_{i,j} \right) / \delta z + \delta t (\rho'_l)^n_{i,j+\frac{1}{2}} g$$

$$+ \delta t \left(r_{i+1} (1 - \alpha^n_{i+\frac{1}{2},j+\frac{1}{2}}) (\sigma_{lrz})^n_{i+\frac{1}{2},j+\frac{1}{2}} - r_{i-\frac{1}{2}} (1 - \alpha^n_{i-\frac{1}{2},j+\frac{1}{2}}) (\sigma_{lrz})^n_{i-\frac{1}{2},j+\frac{1}{2}} \right) / r_i \delta r$$

$$+ \delta t \left((1 - \alpha^n_{i,j+1}) (\sigma_{lzz})^n_{i,j+1} - (1 - \alpha^n_{i,j}) (\sigma_{lzz})^n_{i,j} \right) / \delta z \tag{5.27}$$

$$(\rho'_g I_g)^{n+1}_{i,j} = (\rho'_g I_g)^n_{i,j} - \delta t \left(\left((\rho'_g)^{n+1} I^n_g u^{n+1}_g r \right)_{i+\frac{1}{2},j} - \left((\rho'_g)^{n+1} I^n_g u^{n+1}_g r \right)_{i-\frac{1}{2},j} \right) / r_i \delta r$$

$$\delta t \left(\left((\rho'_g)^{n+1} I^n_g v^{n+1}_g \right)_{i,j+\frac{1}{2}} - \left((\rho'_g)^{n+1} I^n_g v^{n+1}_g \right)_{i,j-\frac{1}{2}} \right) / \delta z$$

$$- p^{n+1}_{i,j} (\alpha^{n+1}_{i,j} - \alpha^n_{i,j}) + \delta t \left((\alpha^{n+1} u^{n+1}_g r)_{i+\frac{1}{2},j} - (\alpha^{n+1} u^{n+1}_g r)_{i-\frac{1}{2},j} \right) / r_i \delta r$$

$$+ \delta t \left((\alpha^{n+1} v^{n+1}_g)_{i,j+\frac{1}{2}} - (\alpha^{n+1} v^{n+1}_g)_{i,j-\frac{1}{2}} \right) / \delta z$$

$$+ \delta t K^n_{i,j} (KG)_{i,j}$$

$$+ \delta t R^n_{i,j} \left((\overline{T}_l)_{i,j} + (T_l)^{n+1}_{i,j} - (\overline{T}_g)_{i,j} - (T_g)^{n+1}_{i,j} \right) / 2 + \delta t \alpha^{n+1}_{i,j} (VG)_{i,j}$$

$$+ \delta t (TKG)_{i,j} \tag{5.28}$$

54

Where,

$$(KG)_{i,j} = \left(\begin{array}{c} \left(u_g^{n+1}{}_{i+\frac{1}{2},j} + u_g^{n+1}{}_{i-\frac{1}{2},j} - u_l^{n+1}{}_{i+\frac{1}{2},j} - u_l^{n+1}{}_{i-\frac{1}{2},j} \right)^2 \\ + \left(v_g^{n+1}{}_{i,j+\frac{1}{2}} + v_g^{n+1}{}_{i,j-\frac{1}{2}} - v_l^{n+1}{}_{i,j+\frac{1}{2}} - v_l^{n+1}{}_{i,j-\frac{1}{2}} \right)^2 \end{array} \right) / 4 \tag{5.29}$$

$$(VG)_{i,j} = \left(\bar{\sigma}_{grr} \right)_{i,j} \left(u_g^{n+1}{}_{i+\frac{1}{2},j} - u_g^{n+1}{}_{i-\frac{1}{2},j} \right) / \delta r$$
$$+ \left(\sigma_{grz} \right)_{i,j} \left(u_g^{n+1}{}_{i+\frac{1}{2},j+1} + u_g^{n+1}{}_{i-\frac{1}{2},j+1} - u_g^{n+1}{}_{i+\frac{1}{2},j-1} - u_g^{n+1}{}_{i-\frac{1}{2},j-1} \right) / 4\delta z$$
$$+ \left(v_g^{n+1}{}_{i+1,j+\frac{1}{2}} + v_g^{n+1}{}_{i+1,j-\frac{1}{2}} - v_g^{n+1}{}_{i-1,j+\frac{1}{2}} - v_g^{n+1}{}_{i-1,j-\frac{1}{2}} \right) / 4\delta r$$
$$+ \left(\sigma_{gzz} \right)_{i,j} \left(v_g^{n+1}{}_{i,j+\frac{1}{2}} - v_g^{n+1}{}_{i,j-\frac{1}{2}} \right) / \delta z + \left(\bar{\sigma}_{g\phi\phi} \right)_{i,j} u_g^{n+1}{}_{i,j} / r_i \tag{5.30}$$

$$(TKG)_{i,j} = \delta t \left(\begin{array}{c} r_{i+\frac{1}{2}} \left(k_g \right)^n{}_{i+\frac{1}{2},j} \alpha^{n+1}{}_{i+\frac{1}{2},j} \left(\left(\bar{T}_g \right)_{i+1,j} - \left(\bar{T}_g \right)_{i,j} \right) \\ - r_{i-\frac{1}{2}} \left(k_g \right)^n{}_{i-\frac{1}{2},j} \alpha^{n+1}{}_{i-\frac{1}{2},j} \left(\left(\bar{T}_g \right)_{i,j} - \left(\bar{T}_g \right)_{i-1,j} \right) \end{array} \right) / r_i \delta r^2$$
$$+ \delta t \left(\begin{array}{c} \left(k_g \right)^n{}_{i,j+\frac{1}{2}} \alpha^{n+1}{}_{i,j+\frac{1}{2}} \left(\left(\bar{T}_g \right)_{i,j+1} - \left(\bar{T}_g \right)_{i,j} \right) \\ - \left(k_g \right)^n{}_{i,j-\frac{1}{2}} \alpha^{n+1}{}_{i,j-\frac{1}{2}} \left(\left(\bar{T}_g \right)_{i,j} - \left(\bar{T}_g \right)_{i,j-1} \right) \end{array} \right) / \delta z^2 \tag{5.31}$$

$$(\rho_l I_l)^{n+1}{}_{i,j} = (\rho_l I_l)^n{}_{i,j} - \delta t \left(\left((\rho_l)^{n+1} I_l^n u_l^{n+1} r \right)_{i+\frac{1}{2},j} - \left((\rho_l)^{n+1} I_l^n u_l^{n+1} r \right)_{i-\frac{1}{2},j} \right) / r_i \delta r$$
$$- \delta t \left(\left((\rho_l)^{n+1} I_l^n v_l^{n+1} \right)_{i,j+\frac{1}{2}} - \left((\rho_l)^{n+1} I_l^n v_l^{n+1} \right)_{i,j-\frac{1}{2}} \right) / \delta z$$
$$- p^{n+1}{}_{i,j} \left(\alpha^n{}_{i,j} - \alpha^{n+1}{}_{i,j} \right)$$
$$+ \delta t p^{n+1}{}_{i,j} \left(\left((1 - \alpha^{n+1}) u_l^{n+1} r \right)_{i+\frac{1}{2},j} - \left((1 - \alpha^{n+1}) u_l^{n+1} r \right)_{i-\frac{1}{2},j} \right) / r_i \delta r$$
$$+ \delta t p^{n+1}{}_{i,j} \left(\left((1 - \alpha^{n+1}) v_l^{n+1} \right)_{i,j+\frac{1}{2}} - \left((1 - \alpha^{n+1}) v_l^{n+1} \right)_{i,j-\frac{1}{2}} \right) / \delta z$$
$$- \delta t R^n{}_{i,j} \left(\left(\bar{T}_l \right)_{i,j} + (T_l)^{n+1}{}_{i,j} - \left(\bar{T}_g \right)_{i,j} - (T_g)^{n+1}{}_{i,j} \right) / 2$$
$$+ \delta t \left(1 - \alpha^{n+1}{}_{i,j} \right) (VL)_{i,j} + \delta t (TKL)_{i,j} \tag{5.32}$$

Where,

$$
\begin{aligned}
(VL)_{i,j} &= (\bar{\sigma}_{lrr})_{i,j}\left(u_l^{n+1}{}_{i+\frac{1}{2},j} - u_l^{n+1}{}_{i-\frac{1}{2},j}\right)/\delta r \\
&+ (\bar{\sigma}_{lrz})_{i,j}\left(u_l^{n+1}{}_{i+\frac{1}{2},j+1} + u_l^{n+1}{}_{i-\frac{1}{2},j+1} - u_l^{n+1}{}_{i+\frac{1}{2},j-1} + u_l^{n+1}{}_{i-\frac{1}{2},j-1}\right)/4\delta z \\
&+ (\bar{\sigma}_{lrz})_{i,j}\left(v_l^{n+1}{}_{i+1,j+\frac{1}{2}} + v_l^{n+1}{}_{i+1,j-\frac{1}{2}} - v_l^{n+1}{}_{i-1,j+\frac{1}{2}} + v_l^{n+1}{}_{i-1,j-\frac{1}{2}}\right)/4\delta r \\
&+ (\sigma_{lzz})_{i,j}\left(v_l^{n+1}{}_{i,j+\frac{1}{2}} - v_l^{n+1}{}_{i,j-\frac{1}{2}}\right)/\delta z + (\bar{\sigma}_{l\phi\phi})_{i,j}\, u_l^{n+1}{}_{i,j}/r_i
\end{aligned}
\tag{5.33}
$$

$$
(TKL)_{i,j} =
\begin{Bmatrix}
r_{i+\frac{1}{2}}(k_l)^n_{i+\frac{1}{2},j}\left(1-\alpha^{n+1}_{i+\frac{1}{2},j}\right)\left((\bar{T}_l)_{i+1,j} - (\bar{T}_l)_{i,j}\right) \\
-r_{i-\frac{1}{2}}(k_l)^n_{i-\frac{1}{2},j}\left(1-\alpha^{n+1}_{i-\frac{1}{2},j}\right)\left((\bar{T}_l)_{i,j} - (\bar{T}_l)_{i-1,j}\right)
\end{Bmatrix}
/ r_i\delta r^2
$$
$$
+
\begin{Bmatrix}
(k_l)^n_{i,j+\frac{1}{2}}\left(1-\alpha^{n+1}_{i,j+\frac{1}{2}}\right)\left((\bar{T}_l)_{i,j+1} - (\bar{T}_l)_{i,j}\right) \\
-(k_l)^n_{i,j-\frac{1}{2}}\left(1-\alpha^{n+1}_{i,j-\frac{1}{2}}\right)\left((\bar{T}_l)_{i,j} - (\bar{T}_l)_{i,j-1}\right)
\end{Bmatrix}
/ \delta z^2
\tag{5.34}
$$

The viscous stress components are discretized using standard central differencing.

$$
\begin{aligned}
(\sigma_{grr})^n_{i+1,j} &= 2(\mu_g)^n_{i+1,j}\left((u_g)^n_{i+\frac{3}{2},j} - (u_g)^n_{i+\frac{1}{2},j}\right)/\delta r \\
&+ (\lambda_g)^n_{i+1,j}\left((u_g)^n_{i+\frac{3}{2},j}\, r_{i+\frac{3}{2}} - (u_g)^n_{i+\frac{1}{2},j}\, r_{i+\frac{1}{2}}\right)/r_{i+1}\delta r \\
&+ (\lambda_g)^n_{i+1,j}\left((v_g)^n_{i+1,j+\frac{1}{2}} - (v_g)^n_{i+1,j-\frac{1}{2}}\right)/\delta z
\end{aligned}
\tag{5.35}
$$

$$
\begin{aligned}
(\sigma_{grz})^n_{i+\frac{1}{2},j+\frac{1}{2}} &= \frac{1}{4}\left((\mu_g)^n_{i,j} + (\mu_g)^n_{i+1,j} + (\mu_g)^n_{i+1,j+1} + (\mu_g)^n_{i,j+1}\right)\left((v_g)^n_{i+1,j+\frac{1}{2}} - (v_g)^n_{i,j+\frac{1}{2}}\right)/\delta r \\
&+ \frac{1}{4}\left((\mu_g)^n_{i,j} + (\mu_g)^n_{i+1,j} + (\mu_g)^n_{i+1,j+1} + (\mu_g)^n_{i,j+1}\right)\left((u_g)^n_{i+\frac{1}{2},j+1} - (u_g)^n_{i+\frac{1}{2},j}\right)/\delta z
\end{aligned}
\tag{5.36}
$$

56

$$\left(u_g\right)_{i+\frac{1}{2},j}^{n+1} = \frac{\left[\begin{array}{l}\left((G)_{i+\frac{1}{2},j} - \delta t\,\alpha_{i+\frac{1}{2},j}^{n+1}\left(P_{i+1,j}^{n+1} - P_{i,j}^{n+1}\right)/\delta r\right)\left((\rho'_l)_{i+\frac{1}{2},j}^{n+1} + \delta t K_{i+\frac{1}{2},j}^{n}\right) \\[2mm] + \delta t K_{i+\frac{1}{2},j}^{n}\left((L)_{i+\frac{1}{2},j} - \left(1-\alpha_{i+\frac{1}{2},j}^{n+1}\right)\delta t\left(P_{i+1,j}^{n+1} - P_{i,j}^{n+1}\right)/\delta r\right)\end{array}\right]}{\left(\rho'_g\right)_{i+\frac{1}{2},j}^{n+1}\left((\rho'_l)_{i+\frac{1}{2},j}^{n+1} + \delta t K_{i+\frac{1}{2},j}^{n}\right) + \delta t K_{i+\frac{1}{2},j}^{n}\left(\rho'_l\right)_{i+\frac{1}{2},j}^{n+1}} \tag{5.40}$$

$$\left(v_g\right)_{i,j+\frac{1}{2}}^{n+1} = \frac{\left[\begin{array}{l}\left((L)_{i,j+\frac{1}{2}} - \delta t\left(1-\alpha_{i,j+\frac{1}{2}}^{n+1}\right)\left(P_{i,j+1}^{n+1} - P_{i,j}^{n+1}\right)/\delta z\right)\left((\rho'_g)_{i,j+\frac{1}{2}}^{n+1} + \delta t K_{i,j+\frac{1}{2}}^{n}\right) + \\[2mm] \delta t K_{i,j+\frac{1}{2}}^{n}\left((G)_{i,j+\frac{1}{2}} - \alpha_{i,j+\frac{1}{2}}^{n+1}\delta t\left(P_{i,j+1}^{n+1} - P_{i,j}^{n+1}\right)/\delta z\right)\end{array}\right]}{\left(\rho'_g\right)_{i,j+\frac{1}{2}}^{n+1}\left((\rho'_l)_{i,j+\frac{1}{2}}^{n+1} + \delta t K_{i,j+\frac{1}{2}}^{n}\right) + \delta t K_{i,j+\frac{1}{2}}^{n}\left(\rho'_l\right)_{i,j+\frac{1}{2}}^{n+1}} \tag{5.41}$$

$$\left(v_g\right)_{i,j+\frac{1}{2}}^{n+1} = \frac{\left[\begin{array}{l}\left((G)_{i,j+\frac{1}{2}} - \delta t\,\alpha_{i,j+\frac{1}{2}}^{n+1}\left(P_{i,j+1}^{n+1} - P_{i,j}^{n+1}\right)/\delta z\right)\left((\rho'_l)_{i,j+\frac{1}{2}}^{n+1} + \delta t K_{i,j+\frac{1}{2}}^{n}\right) + \\[2mm] \delta t K_{i,j+\frac{1}{2}}^{n}\left((L)_{i,j+\frac{1}{2}} - \left(1-\alpha_{i,j+\frac{1}{2}}^{n+1}\right)\delta t\left(P_{i,j+1}^{n+1} - P_{i,j}^{n+1}\right)/\delta z\right)\end{array}\right]}{\left(\rho'_g\right)_{i,j+\frac{1}{2}}^{n+1}\left((\rho'_l)_{i,j+\frac{1}{2}}^{n+1} + \delta t K_{i,j+\frac{1}{2}}^{n}\right) + \delta t K_{i,j+\frac{1}{2}}^{n}\left(\rho'_l\right)_{i,j+\frac{1}{2}}^{n+1}} \tag{5.42}$$

The discrepancies in continuity equations can be written as [4].

$$\left(D_g\right)_{i,j}^{n+1} = \left(\left(\rho'_g\right)_{i,j}^{n+1} - \left(\rho'_g\right)_{i,j}^{n}\right) + \left(\left(\left(\rho'_g\right)u_g r\right)_{i+\frac{1}{2},j}^{n+1} - \left(\left(\rho'_g\right)u_g r\right)_{i-\frac{1}{2},j}^{n+1}\right)\delta t / r_i \delta r$$

$$+ \left(\left(\left(\rho'_g\right)v_g\right)_{i,j+\frac{1}{2}}^{n+1} - \left(\left(\rho'_g\right)v_g\right)_{i,j-\frac{1}{2}}^{n+1}\right)\delta t / \delta z \tag{5.43}$$

$$\left(D_l\right)_{i,j}^{n+1} = \left(\left(\rho'_l\right)_{i,j}^{n+1} - \left(\rho'_l\right)_{i,j}^{n}\right) + \left(\left(\left(\rho'_l\right)u_l r\right)_{i+\frac{1}{2},j}^{n+1} - \left(\left(\rho'_l\right)u_l r\right)_{i-\frac{1}{2},j}^{n+1}\right)\delta t / r_i \delta r$$

$$+ \left(\left(\left(\rho'_l\right)v_l\right)_{i,j+\frac{1}{2}}^{n+1} - \left(\left(\rho'_l\right)v_l\right)_{i,j-\frac{1}{2}}^{n+1}\right)\delta t / \delta z \tag{5.44}$$

There is no separate equation for pressure calculations; so pressure has been adjusted iteratively using Newton-Rapshon method over continuity equations in order to keep the values of (D_g) and (D_l) below a specified convergence criterion in each cell [3, 4 and 7]. If void-fraction is more than 0.1 (α^c), pressure has been iterated over *liquid pressure correction equation* otherwise *gas pressure correction equation* is used in iterative explicit way, i.e. implicit. The value of α^c does not affect the nature of solution although it may have some effects on convergence rate. Convergence will be faster when it will be iterated over liquid continuity equation, because liquid has higher acoustic velocity. The final purpose of pressure iteration is to obtain a pressure field for which the discrepancies in continuity equations are at minimum (compatible with convergence criterion). However instead of achieving full convergence in single iteration, $(1-\beta)$ times of previous iteration values of $(D_l)_{i,j}$ and $(D_g)_{i,j}$ are achieved. In the present work over-relaxation is used $(\beta = 1.5)$.

Convergence criterion is given below,

$$\left(D_g\right)_{i,j} \text{ or } \left(D_l\right)_{i,j} \leq \begin{cases} 10^{-5}\left(\rho'_l\right)_{i,j} & for \ \alpha_{i,j}^n < \alpha^c \\ 10^{-5}\left(\rho'_g\right)_{i,j} & for \ \alpha_{i,j}^n \geq \alpha^c \end{cases} \tag{5.45}$$

Newton-Rapshon Equation or *liquid and gas pressure correction equations* for pressure correction are given as,

$$\left(P_{i,j}\right)^{new} = \left(P_{i,j}\right)^{old} - \left(D_l\right)^{n+1}_{i,j} / \left(\frac{\partial\left(D_l\right)_{i,j}}{\partial P_{i,j}}\right)$$

or

$$\left(P_{i,j}\right)^{new} = \left(P_{i,j}\right)^{old} - \left(D_g\right)^{n+1}_{i,j} / \left(\frac{\partial\left(D_g\right)_{i,j}}{\partial P_{i,j}}\right) \tag{5.46}$$

Now, to accomplish the derivation of $\left(\frac{\partial\left(D_g\right)_{i,j}}{\partial P_{i,j}}\right)$ and $\left(\frac{\partial\left(D_l\right)_{i,j}}{\partial P_{i,j}}\right)$ it is considerably more convenient to differentiate a slightly different expression for $\left(D_l\right)^{n+1}_{i,j}$ and $\left(D_g\right)^{n+1}_{i,j}$, namely the form obtained when the mass convection is derived from a strict centered differencing, with no propagation of donor-cell fluxing [4]. The converged solution is independent of $\left(\frac{\partial\left(D_g\right)}{\partial P_{i,j}}\right)$ and $\left(\frac{\partial\left(D_l\right)_{i,j}}{\partial P_{i,j}}\right)$, it is entirely acceptable to use any desired set of values for this coefficient, provided that the resulting convergence rate is not adversely affected. In many cases, it is sufficient to calculate the values only at the start of the iteration, and keep them fixed throughout the cycle at those initial values. However this arbitrariness does not apply to the specification of $\left(D_l\right)^{n+1}_{i,j}$ and $\left(D_g\right)^{n+1}_{i,j}$, in this case, forms must be exactly as specified in Eq-(5.43) and (5.44). Now using Eqs-(5.19), (5.20), (5.22), (5.23), (5.43), and (5.44) $\left(\frac{\partial\left(D_g\right)_{i,j}}{\partial P_{i,j}}\right)$ and $\left(\frac{\partial\left(D_l\right)_{i,j}}{\partial P_{i,j}}\right)$ are calculated and are given below [4].

60

$$\left(\frac{\partial (D_g)_{i,j}}{\partial P_{i,j}}\right) = 1/(A_g)_{i,j} + \left(r_{i+\frac{1}{2}}\alpha^n_{i+\frac{1}{2},j} + r_{i-\frac{1}{2}}\alpha^n_{i-\frac{1}{2},j}\right)(\delta t)^2 / r_i(\delta r)^2$$

$$+ r_{i+\frac{1}{2}}K^n_{i+\frac{1}{2},j}\frac{\partial\left\{(u_l)^n_{i+\frac{1}{2},j} - (u_g)^n_{i+\frac{1}{2},j}\right\}}{\partial P_{i,j}}(\delta t)^2 / r_i\delta r$$

$$r_{i-\frac{1}{2}}K^n_{i-\frac{1}{2},j}\frac{\partial\left\{(u_l)^n_{i-\frac{1}{2},j} - (u_g)^n_{i-\frac{1}{2},j}\right\}}{\partial P_{i,j}}(\delta t)^2 / r_i\delta r + \left(\alpha^n_{i,j+\frac{1}{2}} + \alpha^n_{i,j-\frac{1}{2}}\right)(\delta t)^2 /(\delta z)^2$$

$$+ K^n_{i,j+\frac{1}{2}}\frac{\partial\left\{(v_l)^n_{i,j+\frac{1}{2}} - (v_g)^n_{i,j+\frac{1}{2}}\right\}}{\partial P_{i,j}}(\delta t)^2 / \delta z$$

$$K^n_{i,j-\frac{1}{2}}\frac{\partial\left\{(v_l)^n_{i,j-\frac{1}{2}} - (v_g)^n_{i,j-\frac{1}{2}}\right\}}{\partial P_{i,j}}(\delta t)^2 / \delta z \qquad (5.47)$$

$$\left(\frac{\partial (D_l)_{i,j}}{\partial P_{i,j}}\right) = 1/(A_l)_{i,j} + \left(r_{i+\frac{1}{2}}\left(1 - \alpha^n_{i+\frac{1}{2},j}\right) + r_{i-\frac{1}{2}}\left(1 - \alpha^n_{i-\frac{1}{2},j}\right)\right)(\delta t)^2 / r_i(\delta r)^2$$

$$+ r_{i+\frac{1}{2}}K^n_{i+\frac{1}{2},j}\frac{\partial\left\{(u_g)^n_{i+\frac{1}{2},j} - (u_l)^n_{i+\frac{1}{2},j}\right\}}{\partial P_{i,j}}(\delta t)^2 / r_i\delta r$$

$$r_{i-\frac{1}{2}}K^n_{i-\frac{1}{2},j}\frac{\partial\left\{(u_g)^n_{i-\frac{1}{2},j} - (u_l)^n_{i-\frac{1}{2},j}\right\}}{\partial P_{i,j}}(\delta t)^2 / r_i\delta r$$

$$+ \left(\left(1 - \alpha^n_{i,j+\frac{1}{2}}\right) + \left(1 - \alpha^n_{i,j-\frac{1}{2}}\right)\right)(\delta t)^2 /(\delta z)^2$$

$$+ K^n_{i,j+\frac{1}{2}}\frac{\partial\left\{(v_g)^n_{i,j+\frac{1}{2}} - (v_l)^n_{i,j+\frac{1}{2}}\right\}}{\partial P_{i,j}}(\delta t)^2 / \delta z$$

$$K^n_{i,j-\frac{1}{2}}\frac{\partial\left\{(v_g)^n_{i,j-\frac{1}{2}} - (v_l)^n_{i,j-\frac{1}{2}}\right\}}{\partial P_{i,j}}(\delta t)^2 / \delta z \qquad (5.48)$$

Where,

$$\left(A_l\right)_{i,j} = \left(1/\left(1-\alpha_{i,j}^{n+1}\right)\right)\left(\frac{\partial P_{i,j}}{\partial\left(\rho_l\right)_{i,j}}\right)_{isentropic} \tag{5.49}$$

$$\left(A_l\right)_{i,j} = \left(1/\left(1-\alpha_{i,j}^{n+1}\right)\right)a_l^2 \tag{5.50}$$

The two above mentioned equations are the general forms for calculating $\frac{\partial(D_l)}{\partial P}$ and $\frac{\partial(D_l)}{\partial P}$. However a simplified form of above equations has been used

in the present analysis as these forms affect the convergence and not the solution.

When void fraction is less than the critical value then iterations are carried out over liquid equations. Liquid metals possess very large values of $\left(A_l\right)_{i,j}$ and $\left(K\right)_{i,j}$. The simplified

form of $\frac{\partial(D_l)}{\partial P}$ can be written as [4],

$$\left(\frac{\partial(D_l)_{i,j}}{\partial P_{i,j}}\right) = 1/\left(\frac{\left(\rho'_l\right)_{i,j}^n \delta r^2 \delta z^2}{2\delta t\left(\delta r^2 + \delta z^2\right)}\right) \tag{5.51}$$

Similarly the change in velocity due to change in pressure in gas, from Eq-(5.47), the

expression for $\left(\frac{\partial(D_g)}{\partial P}\right)$ is calculated as [4],

$$\left(\frac{\partial(D_g)_{i,j}}{\partial P_{i,j}}\right) = 1/\left(A_g\right)_{i,j} + \left(r_{i+\frac{1}{2}}\alpha_{i+\frac{1}{2},j}^n + r_{i-\frac{1}{2}}\alpha_{i-\frac{1}{2},j}^n\right)\left(\delta t\right)^2 / r_i\left(\delta r\right)^2$$
$$+ \left(\alpha_{i,j+\frac{1}{2}}^n + \alpha_{i,j-\frac{1}{2}}^n\right)\left(\delta t\right)^2 / \left(\delta z\right)^2 \tag{5.52}$$

Where,

$$\left(A_g\right)_{i,j} = \left(1/\alpha_{i,j}^{n+1}\right)\left(\frac{\partial P_{i,j}}{\partial\left(\rho_g\right)_{i,j}}\right)_{isentropic} \tag{5.53}$$

$$\left(A_g\right)_{i,j} = \left(1/\alpha_{i,j}^{n+1}\right)a_g^2 \tag{5.54}$$

62

To calculate the void fraction in each cell, if $\alpha_{i,j}^n < \alpha^C$ then

$$\alpha_{i,j}^{n+1} = \left(\rho_g^{'}\right)_{i,j}^{n+1} / \left(\bar\rho_g\right)_{i,j} \tag{5.55}$$

And if $\alpha_{i,j}^n > \alpha^c$ then

$$\alpha_{i,j}^{n+1} = 1 - \left(\rho_l^{'}\right)_{i,j}^{n+1} / \left(\bar\rho_l\right)_{i,j} \tag{5.56}$$

To handle the interfacial energy transfer implicitly intermediate temperatures are defined like,

$$\tilde{T}_l = T_l^n + \left(\bar{I}_l - \left(I_l\right)^n\right)/\left(C_l\right)^n \tag{5.57}$$

$$\tilde{T}_g = T_g^n + \left(\bar{I}_g - \left(I_g\right)^n\right)/\left(C_g\right)^n \tag{5.58}$$

The interfacial heat transfer is equally divided between the calculations of $\bar{I}_g$, $\bar{I}_l$ and final calculation of $\left(I_g\right)^{n+1}$, $\left(I_g\right)^{n+1}$.

I_g and I_l are calculated during explicit iterative pressure calculations only considering energy caused by interfacial drag and half of interfacial heat transfer. With known $\bar{I}_g$ and I_l, densities and temperature of both the phases can be calculated using their equation of states.

The terms for I_g and I_l are given as,

$$\left(I_g\right)_{i,j} = \left(\begin{array}{l} 2\left(c_g^{'}\right)_{i,j}^n \left(C_l\right)_{i,j}^n \left(\rho_l^{'}\right)_{i,j}^{n+1}\left(\left(I_g\right)_{i,j}^n \left(\rho_g^{'}\right)_{i,j}^{n+1} + \delta t(EDRAG)\right) \\ + 2\left(c_g^{'}\right)_{i,j}^n \left(C_l\right)_{i,j}^n \left(\rho_l^{'}\right)_{i,j}^{n+1}\delta t R_{i,j}^n \left(\begin{array}{l}\left(T_l\right)_{i,j}^n - \left(I_l\right)_{i,j}^n /\left(C_l\right)_{i,j}^n \\ -\left(T_g\right)_{i,j}^n + \left(I_g\right)_{i,j}^n /\left(C_g\right)_{i,j}^n\end{array}\right)/2 \\ + \left(c_g^{'}\right)_{i,j}^n \delta t R_{i,j}^n \left(\delta t(EDRAG) + \left(I_l\right)_{i,j}^n \left(\rho_l^{'}\right)_{i,j}^{n+1} + \left(I_g\right)_{i,j}^n \left(\rho_g^{'}\right)_{i,j}^{n+1}\right) \end{array}\right)$$
$$/ \left(\left(c_g^{'}\right)_{i,j}^n \left(\rho_g^{'}\right)_{i,j}^{n+1}\left(2\left(C_l\right)_{i,j}^n \left(\rho_l^{'}\right)_{i,j}^{n+1} + \delta t R_{i,j}^n\right) + \delta t R_{i,j}^n \left(C_l\right)_{i,j}^n \left(\rho_l^{'}\right)_{i,j}^{n+1}\right) \tag{5.59}$$

$$(EDRAG) = K_{i,i}^n \left(\begin{array}{c} \left((u_g)_{i+\frac{1}{2},j}^{n+1} + (u_g)_{i-\frac{1}{2},j}^{n+1} - (u_l)_{i+\frac{1}{2},j}^{n+1} - (u_l)_{i-\frac{1}{2},j}^{n+1} \right)^2 \\ + \left((v_g)_{i,j+\frac{1}{2}}^{n+1} + (v_g)_{i,j-\frac{1}{2}}^{n+1} - (v_l)_{i+\frac{1}{2},j}^{n+1} - (v_l)_{i,j-\frac{1}{2}}^{n+1} \right)^2 \end{array} \right) \tag{5.60}$$

$$(I_l)_{i,j} = 2(C_l)_{i,i}^n \left((I_l)_{i,i}^n (\rho_l^\cdot)_{i,i}^{n+1} - \delta t R_{i,j}^n \left(\begin{array}{c} (T_l)_{i,j}^n - (I_l)_{i,j}^n /(C_l)_{i,i}^n \\ - (T_g)_{i,j}^n + (I_g)_{i,j}^n /(C_g)_{i,j}^n \end{array} \right) / 2 \right)$$
$$\Big/ \left(2(C_l)_{i,i}^n (\rho_l^\cdot)_{i,i}^{n+1} + \delta t R_{i,i}^n \right)$$
$$+ (C_l)_{i,i}^n \delta t R_{i,i}^n (\tilde{I}_g)_{i,j} /(C_g)_{i,j}^n / \left(2(C_l)_{i,j}^n (\rho_l^\cdot)_{i,j}^{n+1} + \delta t R_{i,j}^n \right) \tag{5.61}$$

Final solution for internal energies is obtained, which accounts for the effect of convection, viscous work, single fluid conduction, and the remaining half of the interfacial heat transfer. Final expressions for internal energies are given below,

$$(I_g)_{i,j}^{n+1} = (C_g)_{i,i}^n \frac{[I_1 + I_2 + I_3]}{I_4} \tag{5.62}$$

Where,

$$I_1 \left\{ \begin{array}{l} (\rho_g^\cdot)_{i,i}^{n+1} (I_g)_{i,i} - (I_g)_{i,i}^n \left((\rho_g^\cdot)_{i,i}^{n+1} - (\rho_g^\cdot)_{i,j}^n \right) \\ (\delta t / \delta r)((CVPG1) - (CG_1) + (CG_2)) \\ - (\delta t / \delta r)((CVPG2) - (CG_3) + (CG_4)) \\ + (\delta t / r_i) \alpha_{i,i}^{n+1} (\bar{\sigma}_{g\Phi\Phi})_{i,i} (u_g)_{i,i}^{n+1} \end{array} \right\} \left((C_l)_{i,j}^n (\rho_l^\cdot)_{i,j}^{n+1} + \delta t R_{i,i}^n \right) \tag{5.63}$$

$$(CVPG1) = \left(\left((\rho_g^\cdot)^{n+1} I_g^n v_g^{n+1} \right)_{i,j+\frac{1}{2}} - \left((\rho_g^\cdot)^{n+1} I_g^n v_g^{n+1} \right)_{i,j-\frac{1}{2}} \right)$$
$$+ P_{i,j}^{n+1} \left(\left((\alpha)^{n+1} v_g^{n+1} \right)_{i,j+\frac{1}{2}} - \left((\alpha)^{n+1} v_g^{n+1} \right)_{i,j-\frac{1}{2}} \right)$$
$$- \alpha_{i,j}^{n+1} (\bar{\sigma}_{grz})_{i,j} \left((u_g)_{i+\frac{1}{2},j+1}^{n+1} + (u_g)_{i-\frac{1}{2},j+1}^{n+1} - (u_g)_{i+\frac{1}{2},j-1}^{n+1} - (u_g)_{i-\frac{1}{2},j-1}^{n+1} \right) / 4$$
$$- \alpha_{i,j}^{n+1} (\bar{\sigma}_{gzz})_{i,j} \left((v_g)_{i,j+\frac{1}{2}}^{n+1} - (v_g)_{i,j-\frac{1}{2}}^{n+1} \right) \tag{5.64}$$

$$(CG_1) = \left(K_g\right)^n_{i,j+\frac{1}{2}} \alpha^n_{i,j+\frac{1}{2}} \left(\left(\overline{T}_g\right)_{i,j+1} - \left(\overline{T}_g\right)_{i,j}\right) / \delta z \tag{5.65}$$

$$(CG_2) = \left(K_g\right)^n_{i,j-\frac{1}{2}} \alpha^n_{i,j-\frac{1}{2}} \left(\left(\overline{T}_g\right)_{i,j} - \left(\overline{T}_g\right)_{i,j-1}\right) / \delta z \tag{5.66}$$

$$(CVPG2) = \left(\left(\left(\rho_g^{\cdot}\right)^{n+1} I_g^n u_g^{n+1} r\right)_{i+\frac{1}{2},j} - \left(\left(\rho_g^{\cdot}\right)^{n+1} I_g^n v_g^{n+1}\right)_{i-\frac{1}{2},j}\right) / r_i$$
$$+ P_{i,j}^{n+1}\left(\left((\alpha)^{n+1} u_g^{n+1} r\right)_{i+\frac{1}{2},j} - \left((\alpha)^{n+1} u_g^{n+1} r\right)_{i-\frac{1}{2},j}\right) / r_i$$
$$- \alpha_{i,j}^{n+1}\left(\sigma_{grz}\right)_{i,j}\left(\left(v_g\right)^{n+1}_{i+1,j+\frac{1}{2}} + \left(v_g\right)^{n+1}_{i+1,j-\frac{1}{2}} - \left(v_g\right)^{n+1}_{i-1,j+\frac{1}{2}} - \left(v_g\right)^{n+1}_{i-1,j-\frac{1}{2}}\right) / 4$$
$$- \alpha_{i,j}^{n+1}\left(\sigma_{grr}\right)_{i,j}\left(\left(u_g\right)^{n+1}_{i+\frac{1}{2},j} - \left(u_g\right)^{n+1}_{i-\frac{1}{2},j}\right) \tag{5.67}$$

$$(CG_3) = r_{i+\frac{1}{2}}\left(K_g\right)^n_{i+\frac{1}{2},j} \alpha^{n+1}_{i+\frac{1}{2},j} \left(\left(\overline{T}_g\right)_{i+1,j} - \left(\overline{T}_g\right)_{i,j}\right) / r_i \delta r \tag{5.68}$$

$$(CG_4) = r_{i-\frac{1}{2}}\left(K_g\right)^n_{i-\frac{1}{2},j} \alpha^{n+1}_{i-\frac{1}{2},j} \left(\left(\overline{T}_g\right)_{i,j} - \left(\overline{T}_g\right)_{i-1,j}\right) / r_i \delta r \tag{5.69}$$

$$I_l = \delta t R^n_{i,j}\left(\begin{array}{l}\left(T_l\right)_{i,j} - \left(\overline{T}_g\right)_{i,j} + \left(\overline{I}_g\right)_{i,j} / \left(C_g\right)^n_{i,j} \\ - \left(I_l\right)_{i,j} / \left(C_l\right)^n_{i,j} - P_{i,j}^{n+1}\left(\alpha_{i,j}^{n+1} - \alpha_{i,j}^n\right)\end{array}\right)\left(2\left(C_l\right)^n_{i,j}\left(\rho_l^{\cdot}\right)^{n+1}_{i,j}\right) / 2 \tag{5.70}$$

$$I_l = \left(\begin{array}{l}\left(\rho_l^{\cdot}\right)^{n+1}_{i,j}\left(I_l\right)_{i,j} - \left(I_l\right)^n_{i,j}\left(\left(\rho_l^{\cdot}\right)^{n+1}_{i,j} - \left(\rho_l^{\cdot}\right)^n_{i,j}\right) \\ - \left(\delta t / \delta z\right)\left((CVPG3) - (CG_5) + (CG_6)\right) \\ - \left(\delta t / \delta r\right)\left((CVPG4) - (CG_7) + (CG_8)\right) \\ + \left(\delta t / r_i\right)\left(1 - \alpha_{i,j}^{n+1}\right)\left(\overline{\sigma}_{l\Phi\Phi}\right)_{i,j}\left(u_l\right)^{n+1}_{i,j}\end{array}\right)\left(\delta t R^n_{i,j}\right) \tag{5.71}$$

$$(CTPG3) = \left(\left(\rho_l^{\cdot}\right)^{n+1} I_l^n v_l^{n+1}\right)_{i,J+\frac{1}{2}} - \left(\left(\rho_l^{\cdot}\right)^{n+1} I_l^n v_l^{n+1}\right)_{i,J-\frac{1}{2}} +$$

$$P_{i,J}^{n+1}\left(\left(1-(\alpha)^{n+1}\right)v_l^{n+1}\right)_{i,J+\frac{1}{2}} - P_{i,J}^{n+1}\left(\left(1-(\alpha)^{n+1}\right)v_l^{n+1}\right)_{i,J-\frac{1}{2}}$$

$$\left(1-\alpha_{i,J}^{n+1}\right)(\bar{\sigma}_{lrz})_{i,J}\left((u_l)_{i+\frac{1}{2},J+1}^{n+1} + (u_l)_{i-\frac{1}{2},J+1}^{n+1} - (u_l)_{i+\frac{1}{2},J-1}^{n+1} - (u_l)_{i-\frac{1}{2},J-1}^{n+1}\right)/4$$

$$\left(1-\alpha_{i,J}^{n+1}\right)(\bar{\sigma}_{lzz})_{i,J}\left((v_l)_{i,J+\frac{1}{2}}^{n+1} - (v_l)_{i,J-\frac{1}{2}}^{n+1}\right) \tag{5.72}$$

$$(CG_5) = (K_l)_{i,J+\frac{1}{2}}^n\left(1-\alpha_{i,J+\frac{1}{2}}^{n+1}\right)\left((\bar{T}_l)_{i,J+1} - (\bar{T}_l)_{i,J}\right)/\delta z \tag{5.73}$$

$$(CG_6) = (K_l)_{i,J-\frac{1}{2}}^n\left(1-\alpha_{i,J-\frac{1}{2}}^n\right)\left((\bar{T}_l)_{i,J} - (\bar{T}_l)_{i,J-1}\right)/\delta z \tag{5.74}$$

$$(CTPG4) = \left(\left(\left(\rho_l^{\cdot}\right)^{n+1} I_l^n u_l^{n+1} r\right)_{i+\frac{1}{2},J} - \left(\left(\rho_l^{\cdot}\right)^{n+1} I_l^n u_l^{n+1} r\right)_{i-\frac{1}{2},J}\right)/r_i$$

$$P_{i,J}^{n+1}\left(\left(\left(1-(\alpha)^{n+1}\right)u_l^{n+1} r\right)_{i+\frac{1}{2},J} - \left(\left(1-(\alpha)^{n+1}\right)u_l^{n+1} r\right)_{i-\frac{1}{2},J}\right)/r_i$$

$$\left(1-\alpha_{i,J}^{n+1}\right)(\bar{\sigma}_{lrz})_{i,J}\left((v_l)_{i+1,J+\frac{1}{2}}^{n+1} + (v_l)_{i+1,J-\frac{1}{2}}^{n+1} - (v_l)_{i-1,J+\frac{1}{2}}^{n+1} - (v_l)_{i-1,J-\frac{1}{2}}^{n+1}\right)/4$$

$$\left(1-\alpha_{i,J}^{n+1}\right)(\bar{\sigma}_{lrr})_{i,J}\left((u_l)_{i+\frac{1}{2},J}^{n+1} - (u_l)_{i-\frac{1}{2},J}^{n+1}\right) \tag{5.75}$$

$$(CG_7) = r_{i+\frac{1}{2}}(K_l)_{i+\frac{1}{2},J}^n\left(1-\alpha_{i+\frac{1}{2},J}^{n+1}\right)\left((\bar{T}_l)_{i+1,J} - (\bar{T}_l)_{i,J}\right)/r_i \delta r \tag{5.76}$$

$$(CG_8) = r_{i-\frac{1}{2}}(K_l)_{i-\frac{1}{2},J}^n\left(1-\alpha_{i-\frac{1}{2},J}^{n+1}\right)\left((\bar{T}_l)_{i,J} - (\bar{T}_l)_{i-1,J}\right)/r_i \delta r \tag{5.77}$$

$$I_4 = \left((C_g)_{i,J}^n\left(\rho_g^{\cdot}\right)_{i,J}^{n+1}\left(2(C_l)_{i,J}^n\left(\rho_l^{\cdot}\right)_{i,J}^{n+1} + \delta t R_{i,J}^n\right) + \delta t R_{i,J}^n (C_l)_{i,J}^n\left(\rho_l^{\cdot}\right)_{i,J}^{n+1}\right) \tag{5.78}$$

66

$$I_5 = (\rho_l)_{i,j} (U_l)_{i,j} - (U_l)_{i,j} ((\rho_l)_{i,j} - (\rho_l)_{i,j})$$
$$- (\delta t / \delta z)((CVPG3) - (CG_5) + (CG_6)) - (\delta t / \delta r)((CVPG4) - (CG_7) + (CG_8))$$
$$+ (\delta t / r_i)(1 - \alpha_{i,j}^{n-1})(\bar{\sigma}_{l\Phi\Phi})_{i,j} (u_l)_{i,j}^{n+1}$$
$$+ P_{i,j}^{n+1}(\alpha_{i,j}^{n+1} - \alpha_{i,j}^n) \tag{5.79}$$

$$(I_l)_{i,j}^{n+1} = (C_l)_{i,j}^n \left(2I_5 - \delta t R_{i,j}^n \left((\bar{T}_l)_{i,j} - (\bar{T}_g)_{i,j} + (\bar{I}_g)_{i,j} / (C_g)_{i,j}^n - (\bar{I}_l)_{i,j} / (C_l)_{i,j}^n\right)\right)$$
$$\left(2(C_l)^n (\rho_l)_{i,j}^{n+1} + \delta t R_{i,j}^n\right)$$
$$+ \left((C_l)^n \delta t R_{i,j}^n (I_g)_{i,j}^{n+1} / (C_g)_{i,j}^n\right) / \left(2(C_l)_{i,j}^n (\rho_l)_{i,j}^{n+1} + \delta t R_{i,j}^n\right) \tag{5.80}$$

The quantities (σ_g) and $(\bar{\sigma}_l)$ are evaluated using time level (n+1) velocities and the time level (n) viscosities.

5.4.3 Solution procedure

The solution procedure step-by-step is given as [4],

1. First set up the initial conditions for P, T_g, T_l, α, u_g, u_l, v_g, and v_l in each cell of computational domain and some constant variables.

2. Calculate initial values of ρ_g, ρ_l, ρ'_g, ρ'_l, I_g, I_l, C_g, and C_l for each cell in computational domain from gas and liquid equation of state (Eqs-(5.96)-(5.102), Eqs-(5.7)-(5.8)).

3. Assign all above evaluated values to n^{th} time level values, and calculate n^{th} time level K_g, K_l, μ_g, μ_l, and acoustic velocities for gas and liquid for each cell.

4. Apply velocity and pressure boundary conditions, like no-slip, free-slip, constant pressure, specified-influx, continuous outflow.

5. Calculate $(L)_{i+\frac{1}{2},j}$, $(L)_{i,j+\frac{1}{2}}$, $(G)_{i+\frac{1}{2},j}$, and $(G)_{i,j+\frac{1}{2}}$ using n^{th} time level quantities, and calculate n^{th} time level K and R (Eqs-(5.24)-(5.27)).

6. Solve the four momentum equations explicitly to calculate the eight velocities, and then using these velocities and n^{th} time level densities calculate mass fluxes (Eqs-(5.39)-(5.42)).

7. For each time step update, from t^n to t^{n+1}

8. For each cell, till all cells have $\left|(D_l)\right|$ or $\left|(D_g)\right| \leq \varepsilon$ simultaneously.

   8.1. Calculate $\left(\dfrac{\partial(D_l)}{\partial P}\right)$, $\left(\dfrac{\partial(D_g)}{\partial P}\right)$ for each cell using n^{th} time level quantities (Eqs-(5.51)-(5.52))

   8.2. Calculate (D_l) for $\alpha^n_{i,j} < \alpha^c$, and (D_g) for $\alpha^n_{i,j} \geq \alpha^c$ (Eq-(5.44)).

   8.3. If $\left|(D_l)\right|$ or $\left|(D_g)\right| \leq \varepsilon$ go to 8.7 for $\alpha^n_{i,j} < \alpha^c$, and to 8.8 for $\alpha^n_{i,j} \geq \alpha^c$.

   8.4. If $\left|(D_l)\right|$ or $\left|(D_g)\right| > \varepsilon$ calculate new pressure using Newton-Rapshon method with over-relaxation (relaxation parameter=1.5) (Eq-(5.46)).

8.5. Calculate $\left(\tilde{I}_g\right)$ and $\left(\tilde{I}_l\right)$ omitting temporarily the effects of convection, work, and single-phase conduction. Evaluate $\bar{\rho}_l$ and $\bar{T}_l$ from liquid equation of state, and $\bar{\rho}_g$ and $\bar{T}_g$ from gas equation of state (Eqs-(5.59) and (5.61)).

8.6. Again calculate the eight velocities namely, $\left(u_l\right)^{n+1}_{i+\frac{1}{2},j}$, $\left(u_l\right)^{n+1}_{i-\frac{1}{2},j}$, $\left(v_l\right)^{n+1}_{i,j+\frac{1}{2}}$, $\left(v_l\right)^{n+1}_{i,j-\frac{1}{2}}$, $\left(u_g\right)^{n+1}_{i+\frac{1}{2},j}$, $\left(u_g\right)^{n+1}_{i-\frac{1}{2},j}$, $\left(v_g\right)^{n+1}_{i,j+\frac{1}{2}}$, and $\left(v_g\right)^{n+1}_{i,j-\frac{1}{2}}$ from momentum equations (Eqs-(5.39)-(5.42)).

8.7. If $\alpha^n_{i,j} > \alpha^l$ calculate mass fluxes for gas.

8.7.1. Solve the gas continuity equation for $\left(\rho'_g\right)^{n+1}_{i,j}$ (Eqs-(5.18)).

8.7.2. Calculate $\alpha^n_{i,j} = \left(\rho'_g\right)^n_{i,j}/\left(\bar{\rho}_g\right)_{i,j}$.

8.7.3. Calculate $\left(\rho'_l\right)^{n+1}_{i,j} = \left(1-\alpha^{n+1}_{i,j}\right)\left(\bar{\rho}_l\right)_{i,j}$

8.7.4. If $\left|\left(D_g\right)\right| < \varepsilon$ go to the next cell.

8.7.5. If $\left|\left(D_g\right)\right| > \varepsilon$ calculate new mass fluxes using the new $\left(\rho'_l\right)^{n+1}_{i,j}$ and velocities and return to 8.1 for new pressure $P^{n+1}_{i,j}$ estimate

8.8. If $\alpha^n_{i,j} > \alpha$ calculate mass fluxes for liquid.

8.8.1 Solve the liquid continuity equation for $\left(\rho'_l\right)^{n+1}_{i,j}$ (Eqs-(5.21)).

8.8.2. Calculate $\alpha^n_{i,j} = 1 - \left(\rho'_l\right)^n_{i,j}/\left(\bar{\rho}_l\right)_{i,j}$.

8.8.3 Calculate $\left(\rho'_g\right)^{n+1}_{i,j} = \alpha^{n+1}_{i,j}\left(\bar{\rho}_g\right)_{i,j}$

8.8.4 If $\left|\left(D_l\right)\right| < \varepsilon$ go to the next cell.

8.8.5. If $\left|\left(D_g\right)\right| > \varepsilon$ calculate new mass fluxes using the new $\left(\rho'_g\right)^{n+1}_{i,j}$ and velocities and return to 8.1 for new pressure $P^{n+1}_{i,j}$ estimate.

9. Calculate $\left(I_g\right)^{n+1}_{i,j}$ and $\left(I_l\right)^{n+1}_{i,j}$ implicitly considering the effects of convection, work, and single-phase conduction, and half of interfacial heat transfer, Evaluate ρ_l and $\left(T_l\right)^{n+1}_{i,j}$ from liquid equation of state, and $\bar{\rho}_g$ and $\left(T_g\right)^{n+1}_{i,j}$ from gas equation of state (Eqs-(5.62) and (5.80)).

69

10. Calculations for one time step update are over return to 7 for next time step, and repeat same.

5.4.4 Interfacial transfer formulations

Interfacial drag coefficient and heat transfer coefficient are the two important parameters governing the actual interface transfer processes and need special attentions. The formulation for interfacial drag coefficient in undistorted particle regime (Viscous regime) has been given below [8, 11, and 12].

$$\dot{M}_{ig} = \frac{\alpha \vec{F}_g}{B_g} + \frac{\alpha \vec{F}_{\Gamma}}{B_g} + \frac{9\alpha}{2r_b} \sqrt{\frac{\rho_l \mu_m}{\pi}} \int_{t}^{\frac{D_g}{D_t}(\vec{v}_l - \vec{v}_g)} \frac{d\xi}{\sqrt{(t-\xi)}} \tag{5.81}$$

Where, $\vec{F}_g$, B_g, $\vec{F}_{\Gamma}$, r_b, and μ_m are the standard drag force, volume of a typical particle, virtual mass force, bubble radius and mixture viscosity, respectively [8, 11, and 12]. In the above formulation first term deals with steady force whereas last two terms deal with transient forces. Basically, the first term consists of *interfacial skin and form drag*. However the second term is *virtual mass force*, when a bubble accelerates then the virtual liquid mass around it also accelerates with the same velocity. Virtual mass force itself consists of two parts, one is transient and other is due to convection of liquid around the bubble. Convection term for virtual mass force has been neglected because of high liquid viscosity. Third term is *Basset force*, which arises from acceleration of viscous boundary layer around the bubble. Boundary layer formation around the bubble has also been neglected; therefore Basset force has been dropped out. An additional force, which is possible, is Faxen force (a viscous contribution), which is the correction applied to virtual mass effect and Basset force to account for fluid velocity gradient. Faxen force has not been considered in the present formulation.

The bubbly flow regime is expected to exist for low void fractions, nearly less than 0.3. Assuming spherical bubble of uniform size the number of bubbles per unit volume is,

$$n_b = 3\alpha / \left(4\pi r_b^3\right) \tag{5.82}$$

r_b, is the radius of a typical bubble.

Interfacial area per unit volume in bubbly flow is defined as [8],

$$A_i = 3\alpha / r_b \tag{5.83}$$

Drag resistance of a single vapor bubble can be written as

$$\bar{F}_b = \frac{1}{2} C_D \rho A |\bar{V}| \bar{V} \tag{5.84}$$

Where C is the resistance coefficient, ρ is the liquid density, A is the typical projected area of a bubble and $\bar{F}$ is the relative velocity vector.
On further simplification,

$$\bar{F}_b = \frac{1}{2} C_D \rho_l \pi r_b^2 |\bar{V}_l - \bar{V}_g| (\bar{V}_l - \bar{V}_g) \tag{5.85}$$

So, the resistance or friction force per unit volume is obtained by multiplying Eq-(5.85) by n [12].

$$\frac{\alpha \bar{F}_g}{B_g} = \frac{3}{8} \frac{\alpha}{r_b} C_D \rho_l |\bar{V}_l - \bar{V}_g| (\bar{V}_l - \bar{V}_g) \tag{5.86}$$

Drag resistance coefficient for the spheres is defined as [12],

$$C_D = \frac{24}{\mathrm{Re}} \left(1 + 0.15 \mathrm{Re}^{0.687} \right) + \frac{0.42}{1 + 4.25 \times 10^4 \, \mathrm{Re}^{-1.16}} \tag{5.87}$$

The Reynolds number is given as,

$$\mathrm{Re} = \frac{2 r_b \rho_l |\bar{V}_l - \bar{V}_g|}{\mu_l} \tag{5.88}$$

Interphase drag coefficient K_i caused by steady forces, is defined as the interphase friction value divided by the difference of phase velocities.

$$K_i \equiv \frac{\dfrac{\alpha \bar{F}_g}{B_g}}{\bar{V}_g - \bar{V}_l} \tag{5.89}$$

$$K_1 = \frac{3}{8}\frac{\alpha}{r_b}\rho_l\left|\vec{V}_l - \vec{V}_g\right|\left[\frac{24}{Re}\left(1 + 0.15\,Re^{0.687}\right) + \frac{0.42}{1 + 4.25\times10^4\,Re^{-1.16}}\right] \quad (5.90)$$

Virtual mass force is given as [12],

$$\frac{\alpha\vec{F}_i}{B_g} = C_{VM}\,\alpha\rho_l\left(\frac{D_g\left(\vec{V}_R\right)}{Dt} - \vec{V}_R \bullet \nabla\vec{V}_l\right) \quad (5.91)$$

$\vec{V}_r = \left(\vec{V}_l - \vec{V}_g\right)$ is the relative velocity between phases, and C_{VM} virtual mass coefficient. Where, the substantial derivative is given as,

$$\frac{D_g(\ )}{Dt} = \frac{\partial(\ )}{\partial t} + \vec{V}_g \bullet \nabla(\ )$$

On further simplification, by neglecting the convective part of virtual mass force and considering purely transient part, term becomes,

$$\frac{\alpha\vec{F}_i}{B_g} = C_{VM}\,\alpha\rho_l\left[\frac{\partial\vec{V}_R}{\partial t}\right] \quad (5.92)$$

Virtual mass coefficient for bubbly flow is given as [8],

$$C_{VM} = \frac{1}{2}\alpha\frac{1+2\alpha}{1-\alpha} \quad (5.93)$$

Then interphase virtual mass coefficient K_2 is defined as,

$$K_2 = \frac{\frac{1}{2}\alpha\left[\frac{1+2\alpha}{1-\alpha}\right]\alpha\rho_l\left[\frac{\partial\vec{V}_R}{\partial t}\right]}{\left|\vec{V}_l - \vec{V}_g\right|} \quad (5.94)$$

$$K = K_1 + K_2 \quad (5.95)$$

Presently very large value of interfacial heat transfer coefficient ($R = 1.0\times10^{20}$) has been taken. It has been assumed that interface does not control the interfacial heat

been found quite efficient for bubbly flows to handle temperature discontinuities.

5.4.5 Numerical stability

Stewart (1979) considered the numerical stabilities of two-fluid model in a quite diversified manner [5]. It was said that two-fluid modeling of two-phase flow may yield a system of partial differential equations having complex characteristics; this results in a mathematically ill-posed initial value problem. The behavior of finite difference equations with and without exchange terms has also been explored by Stewart [5]. Two-fluid finite difference formulations without interfacial exchange term have been considered first and it was concluded that if the convective limit (courant number [6], with convection propagation, not sonic propagation) on the time step is obeyed, the highest frequency modes (wavelength small multiple of cell dimension) should not grow geometrically, even for the ill-posed two-fluid problem. Now turning to low frequency modes, time and space step should not be too small.

With momentum exchange considerations, it was shown that the product of momentum exchange coefficient and space step should not be too small. Moreover, partial donor cell differencing of convective fluxes contributes mitigating positive diffusive term and makes the numerical technique stable enough.

At present in bubbly flow, having large momentum exchange, suitable value of space step has been taken to assure stability. Appropriate time step has been taken (neither too large nor too small) based upon convective courant number because of explicit handling of convective terms in momentum equations [6, 5].

5.5 Modeling of LBE-Argon system

The liquid metal two-phase flow system considered is a lead-bismuth and argon gas two-phase flow. Calculations have been carried out in a two-dimensional Cartesian coordinate system, dividing the 20×20 square cm test field into 23×23 grids, including fictitious cells. All the discritized equations governing the complex microphysics of two-phase flow have been solved using point-by-point gauss siedel method with over relaxation in pressure correction using Newton-Rapshon method. LBE (Lead-Bismuth Eutectic) and argon gas are entering at the bottom and are leaving out from the top of the physical domain, a square obstacle has been considered at the centre of the physical domain. Its Schematic has been given below (Fig-5.2).

Schematic of the physical domain

Fig-5.2 Physical and computational Domain

Eulerian cells have been used with cell sizes $\Delta X = 0.95$ cm, $\Delta Y = 0.95$ cm and $\Delta t = 1.5 \times 10^{-4}$ sec. Time step has been taken based upon iterative pressure corrections, by ensuring that with a single iteration during pressure correction, fluid should not travel more than one cell (courant stability criterion). Iterative explicit technique during pressure correction facilitates nearly implicit treatment of momentum equation for sonic propagation. However, convective terms are handled explicitly and therefore limit the stability on convective propagation. Thus ICE allows higher time step than pure explicit technique [3]. Calculations have been done without gravity.

5.5.1. Boundary conditions

The boundary conditions have been enforced by considering fictitious cells surrounding the computing mesh.

5.5.2. No-slip boundary condition on a wall

For rigid walls, the tangential velocities in fictitious cells are set by the reflection with a change in sign. However, normal velocity has been taken zero.

5.5.3. Continuous outflow boundary

Continuous out-flow boundaries are gradient free in their normal direction.

5.5.4. Specified inflow boundary

X and Y components of velocities are defined.

For initial conditions, the whole physical domain has been considered mostly filled with LBE (void fraction 0.05) at 1.0×10^6 dynes/cm^2 pressure and 403 K temperature. At t=0 sec liquid and gas both are introduced at the bottom with v=10 cm/sec, u=0.0 cm/sec at 1.0×10^6 dynes/cm^2 and 403 K temperature with void fractions=0.3.

Due to undistorted particle or viscous regime consideration, bubble radius has been assumed constant throughout the flow and value used in all calculations is 0.20 cm. For simplicity, the interfacial heat transfer coefficient R is set to large constant values i.e. very tight coupling is assumed in terms of heat transfer. (i.e. temperatures of both liquid and gas are equal) or in other words entropy production at the interface is assumed zero [2, 4]. High values of R and K work ideally with highly dispersed flows, but if the flow regime changes from dispersed to separate or some other regime then this is not a good assumption. In that case, both R and K need special attentions.

5.6 Thermo-physical properties of the LBE-Argon system

Relationships for the Lead-Bismuth physical properties are given below [47],

$$Density \quad (gm/cm^3) = 10.737 - 1.375 \times 10^{-3} T_{LBE} \qquad (5.96)$$

$$Thermal \quad conductivity \quad (ergs/sec\,cm\,°C) = 7.26 \times 10^5 + 1.23 \times 10^3 T_{LBE} \qquad (5.97)$$

$$\textit{Specific heat } (ergs/gm^oC) = 1.465 \times 10^6 \qquad (5.98)$$

$$\textit{Dynamic viscosity } (gm/cm\,sec) = 3.26 \times 10^{-2} - 6.26 \times 10^{-5} T_{LBE} + 4.63 \times 10^{-8} T_{LBE}^2 \quad (5.99)$$

Relationships for the Argon gas physical properties are given below [48, 49],

$$\textit{Density } (gm/cm^3) = (P/RT)m_w \qquad (5.100)$$

$$\begin{aligned}\textit{Thermal conductivity } &(ergs/\sec cm^oC)\\ (1632.74 &+ 4.474 T_{AR} - 1.725 \times 10^{-3} T_{AR}^2 + 5.528 \times 10^{-7} T_{AR}^3)\end{aligned} \qquad (5.101)$$

$$\textit{Specific heat } (ergs/gm^oC) = 5.207 \times 10^6 \qquad (5.102)$$

The relationship of dynamic viscosity of Argon gas with temperature has been utilized from PERRY'S CHEMICAL ENGINEER'S HANDBOOK [49].

Reference Temperature (Kelvins) 403

Reference pressure (dynes/cm^2) 1×10^6

Where, temperatures T_{LBE} or T_{AR} are in ^oC, and pressure (P) in dynes/cm^2.

Chapter 6

Results and discussions on LBE-Argon simulations

Above mentioned geometry has been solved and results are reported at T=0.75, T=1.5, T 3.0, and T 4.5 sec with Δt=0.00015 sec, Fig-6.1-6.4 gives the void fraction patterns at three real time levels.
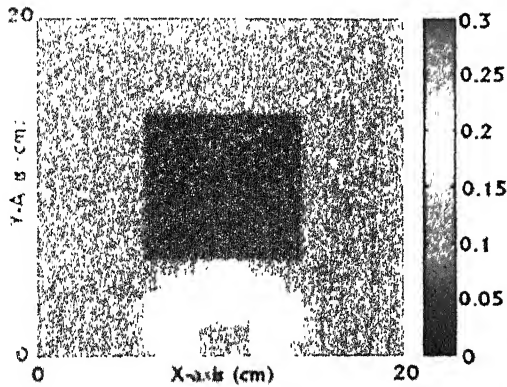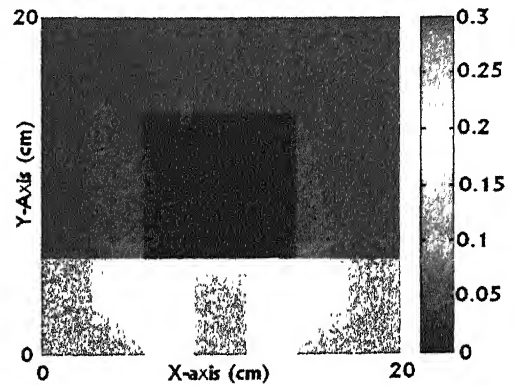

Fig-6.1 Void-fraction patterns at t=0.75 sec
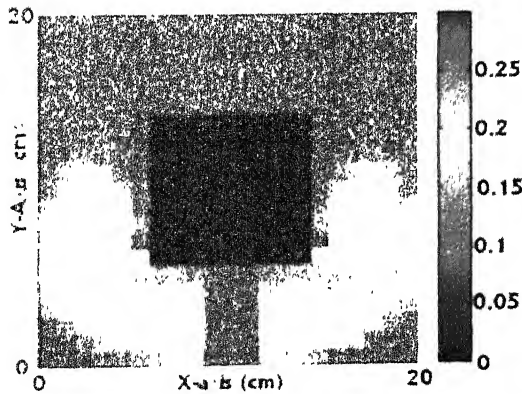

Fig-6.2 Void-fraction patterns at t=1.5 se
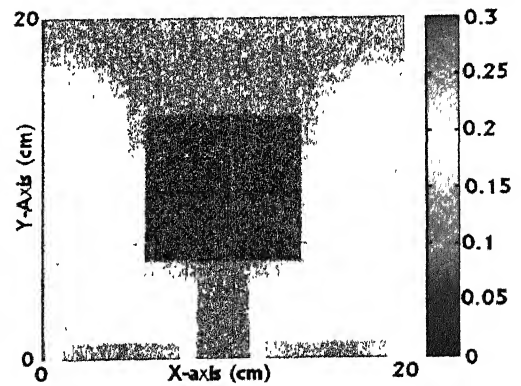

Fig-6.3 Void-fraction patterns at t=3.0 sec

Fig-6.4 Void-fraction patterns at t=4.5 sec

Because of utilizing staggered grids in the formulations, both the velocity components are not defined at the same location. So to plot velocity vectors linear interpolations have been done to define both the velocity components at centre of the cells. Fig-6.5-6.8 represents the velocity vectors of both the fields at three time levels.
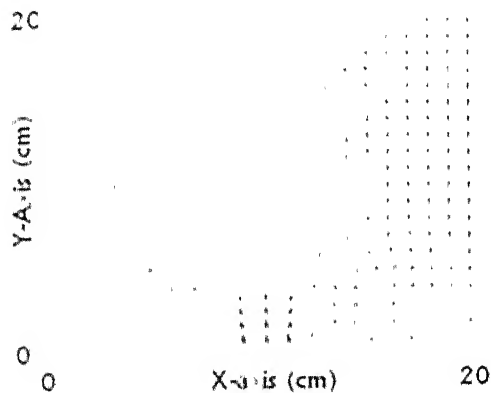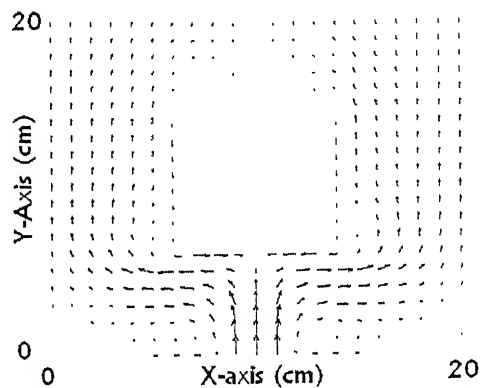

Fig 6.5 Gas velocity vectors at t=0.75 sec
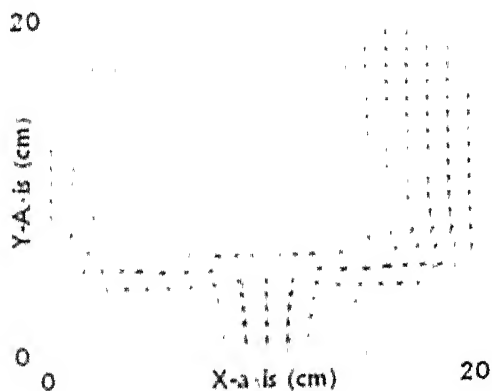

Fig-6.6 Gas velocity vectors at t=1.5 sec
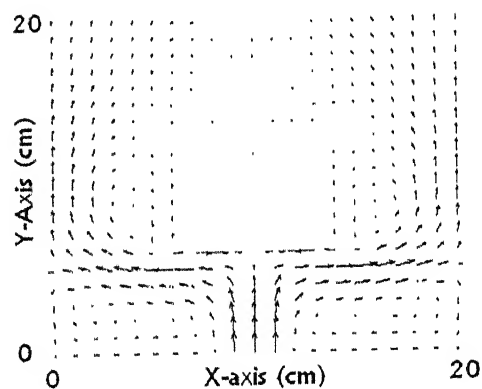

Fig 6.7 Gas velocity vectors at t=3.0 sec

Fig-6.8 Gas velocity vectors at t=4.5 sec

Fig-6.9-6.12 represents the liquid velocity vectors in the physical domain at three time levels. From all above presented velocity vectors it can be seen that enough equality exist between the gas and liquid velocities, thus verifies the actual dynamics and enough realistic formulations of interfacial drag of bubbly flows.

Both the fluids are entering at the bottom and show smooth velocity profiles, as time increases the formation of eddies in the corner locations takes place and velocity vectors are compatible enough with void fraction patterns for realistic bubbly flows.
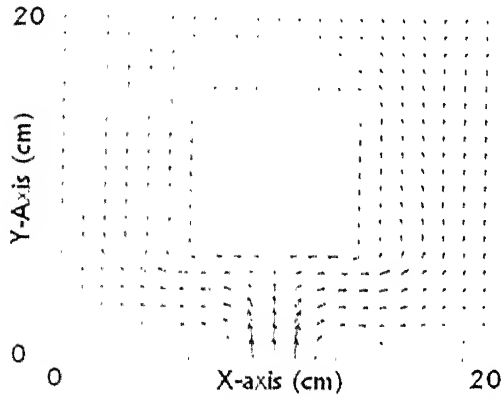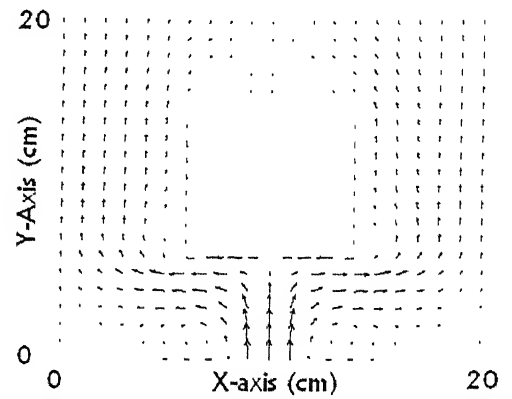
Fig-6.9 Liquid velocity vectors at t=0.75 sec

Fig-6.10 Liquid velocity vectors at t=1.5 sec
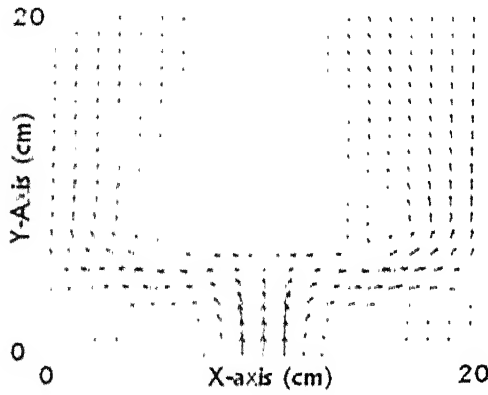
Fig-6.11 Liquid velocity vectors at t=3.0 sec
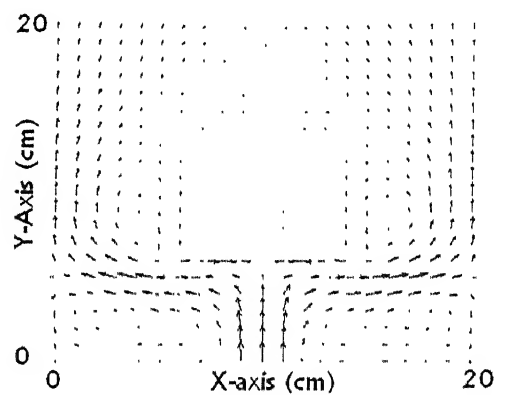
Fig-6.12 Liquid velocity vectors at t=4.5 sec

Solution of energy equations, with assumption of no entropy production at interfaces also has agreement with actual bubbly flows. Small temperature variations down the flow have been reported. Temperature values of both the fields are nearly same and are in agreement with bubbly flows with higher R.

Initial conditions play a crucial role in actual two-phase flow stabilities; these may be uniform or non-uniform but should not have discontinuities. LBE is a high-density fluid

with strong hydrostatic pressure variations, so for tall structural simulations in liquid metal specifically, non-uniform initial conditions are recommended. Presently uniform initial conditions have been employed in absence of gravity.

Chapter 7

Conclusions and future scope

Gamma ray attenuation technique with suitable tomographic inversion algorithms and two-fluid simulations of liquid metal two-phase flows are having different result sets. Two-fluid modeling has shown superiority in terms of result sets; along with void distributions it gives pressure and velocity profiles. Conclusions on both the techniques based upon the present work have been drawn.

7.1 Tomographic algorithms

First conclusions are drawn over tomographic algorithms suitable for corrupted void fraction projection data, based upon the studies carried out it can be said that GH MART, Lent MART, minimum energy and Simple ART algorithms have given encouraging results for constant field reconstructions.

Minimum energy method gives minimum error in step and impulse field reconstructions, and spans enough range of relaxation parameter (almost whole possible range). The error levels in GBH MART and maximum entropy method have been reported at maximum. Initial guess of the field values in these tomographic algorithms have their own importance; different initial guesses may give different error levels in reconstructions. Studies related to initial guess are due and can be extended in future work.

Gamma-ray attenuation technique can be used to collect projection data on ADS leg followed by their inversion in void fraction distributions.

7.2 Two-fluid simulations

In addition to void fraction distributions, two-phase flow modeling gives velocities, pressure drops, etc. Two-fluid modeling of LBE-Argon in a simple geometry has enough agreement with realistic pure bubbly flows. Still the experimental verification is required to verify the results of two-fluid simulations for its further application over gas-driven ADS target systems.

In the present literature, formulations of interfacial transport terms are just limited to pure bubbly flow; this limitation can be extended to apply the same model with same solution procedure over other flow regimes (like slug, churn turbulent, annular flows), with change in interfacial coupling terms. This is a two-fluid single pressure model; and can be updated to a two-pressure model to deal gas and liquid separately in terms of pressure. Initial conditions also play a crucial role in real two-phase stabilities; non-uniform initial conditions should be employed without any discontinuity. For tall structural simulations, non-uniform initial conditions are desirable because of strong hydrodynamic pressure in liquid metals. No coalescence or disintegration of the bubbles has been accounted. The bubble tracking equation can also be coupled with present six field equations to account for coalescence etc. In interfacial heat transfer calculations, tight coupling between two fields, in agreement of pure bubbly flows, is assumed with high interfacial heat transfer coefficient (very small interfacial thickness, no entropy production at interfaces). But if flow regime changes from bubbly to annular etc., then proper analytical model for interfacial heat transfer should be considered. Turbulence modeling can also be added in the present formulation to extend the model for turbulent two-phase flows.

Here implementations have been done on a simple geometry for demonstration purpose; however studies are due on actual ADS target module geometry considering gravity and transient inflow boundary conditions to accommodate the actual gravity dominating ADS loop flow.

At last, it can be said that gamma ray attenuation technique with suitable tomographic inversion algorithms can also be used to verify the results of two-fluid simulations.

References

[1] **Biswas, G., and Munshi, P.** 'Experimental investigation of the LMMHD facility at BARC using techniques of computerized tomography', Final project report submitted to BRNS, DAE (2001).

[2] **Ishi, M.** Thermo-Fluid Dynamic Theory of Two-phase Flow, collection de la direction des Etudes et recherches d'Electricite de France, Eyrolles, Paris (1975).

[3] **Harlow, F. H., and Amsden, A. A.** "A numerical fluid dynamics calculation method for all flow speeds", J. Computational Phys. 8 (1971) pp 197-213.

[4] **Harlow, F. H., and Amsden, A. A.** "Numerical calculation of multiphase fluid flow", J. Computational Phys. 17 (1975) pp 19-52.

[5] **Stewart, B. H.,** "Stability of two-phase flow calculations using two-fluid models", J. Computational Phys. 33 (1979) pp 259-270.

[6] **Hirt, C. W.,** "Heuristic stability theory for finite-difference equations", J. Computational Phys. 2 (1968) pp 339-355.

[7] **Harlow, F. H., and Amsden., A. A.** "Flow of interpenetrating material phases", J. Computational Phys. 18 (1975) pp 440-464.

[8] **Ishii, M., and Mishima K.,** "Two-fluid model and hydrodynamic constitutive relations", Nuclear Eng. and Design 82 (1984) pp 107-126.

[9] **Hetsroni, G.,** Handbook of multiphase systems, Hemisphere Pub. Corp., McGraw-Hill (1982).

[10] Satyamurthy, P., and Venkatramani, N., "Thermal-hydraulic issues related to spallation neutron targets of accelerator Driven Sub-critical Nuclear Reactors", International Symposium on Recent Trends in Heat and Mass Transfer, IIT Guwahati, January 6-8, India, 2002.

[11] Kocamustafaogullaria, G., and Ishii, M., "Foundation of the interfacial area transport equation and its closure relations", Int. J. Heat & Mass Transfer 38, No 3 (1995) pp 418-493.

[12] Jones, A. V., Modelling and solution techniques for multiphase flow (Proceedings of workshop held at Joint Research Centre, Ispra (Italy) Nov. 18-25, 1985), Harwood Academic Publishers, 1985.

[13] Tannehill, C. J., Anderson, A. D., and Pletcher, H. R., Computational fluid mechanics and heat transfer, Taylor & Francis Publishers, 2nd Edition (1997).

[14] Thiyagarajan, T. K., Dixit, N. S., Satyamurthy, P., Venkatramani, N., and Rohatgi, V. K., "Gamma-ray attenuation method for void fraction measurement in fluctuating two-phase liquid metal flows", Measure. Sci. Tech. 2 (1991) pp 64-79.

[15] Munshi, P., Jayakumar, P., Satyamurthy, P., Thiyagarajan, T. K., Dixit, N. S., Venkatramani, N., "Void-fraction measurements in a steady-state mercury-nitrogen flow loop", Experiments in fluids 24 (1998) pp 424-430.

[16] Thiyagarajan, T. K., Satyamurthy, P., Dixit, N. S., Venkatramani, N., Garg, A., and Kanvinde, N. R., "Void-fraction profile measurements in two-phase mercury-nitrogen flows using gamma-ray attenuation method", Experimental thermal and fluid Sc. 10 (1995) pp 347-354.

[17] Satyamurthy, P., and Biswas, K., "Design of a LBE spallation target for fast-thermal accelerator driven sub-critical system (ADS)", Seventh Information Exchange

[18] **Biswas, K., and Satyamurthy, P.,** "Coolant circuit design for a heavy liquid metal spallation target in an accelerator driven sub-critical reactor system", International Symposium on Recent Trends in Heat and Mass Transfer, IIT Guwahati, January 6-8, India, 2002.

[19] **Rubbia et al.,** CERN – Group conceptual design of a fast neutron operated high power energy amplifier, Accelerator Driven Systems: Energy generation and transmutation of nuclear waste, status report, IAEA – TECDOC-985, November 1997.

[20] A roadmap for developing ATW technology: Target and Blanket System, LAUR-3022, Los Alamos National Laboratory, USA, September, 1999.

[21] A European roadmap for developing Accelerator Driven Systems (ADS) for Nuclear Waste Incineration, The European technical Working Group on ADS, April, 2001.

[22] Roadmap for the development of accelerator driven sub-critical reactor systems (ADS) - An interim report of the co-ordination committee on ADS, BARC/2000/R/004, Mumbai, India, 2001.

[23] **Dewekar, S. B., Sahni, D. C., and Kapoor, S. S.,** "Analysis of a high gain energy amplifier based on the way coupled booster reactor concept", International conference on Sub-Critical Accelerator Driven Systems, Moscow, Russia, October 11-15, 1999.

[24] **Shedov et al.,** ADS program in Russia, Accelerator Driven Systems: Energy generation and transmutation of nuclear waste, Status Report, IAEA-TECDOC-985, November 1997.

[25] Interim report on the technical working group on Accelerator Driven Sub-critical Systems, CERN Internal Report, October 12, 1998.

[26] MYRRHA – A multipurpose Accelerator Driven System for Research & Development, IAEA-AGM on "Design and performance of reactor and Sub-critical Systems cooled by Pb-Bi", Moscow, October-2000.

[27] Energy Amplifier Demonstration facility Reference Configuration-Summary Report, EA B0.00 1 200-Rev.0, Italy.

[28] High Power Spallation Target, EADF Report, ANSALDO, Italy.

[29] **Knebel, U. J. I.,** (Project Coordinator), Thermal hydraulic and material specific investigations into the realization of an Accelerator driven System (ADS), HGF Strategy fund project 99/16, Forschungzentrum Karlsruhe, Institute for Kern and Energietechnik, Karlsruhe, Germany, 1999.

[30] **Subbarao, P., Munshi, P., and Muralidhar, K.,** "Performance of iterative tomographic algorithms applied to non-destructive evaluation with limited data", NDT & E International, 30 No. 6 (1997) pp 359-370.

[31] **Gull, S. F.,** "Maximum Entropy tomography", Appl. Opt. 25 (1986) pp 156-160.

[32] **Mayinger, F.,** "Optical Measurements", Springer-Verlag, New York, 1994.

[33] **Gordon, R., Bender, R., and Herman, G. T.,** "Algebraic reconstruction technique (ART) for three-dimensional electron microscopy and X-ray photography", J. Theo. Biol. 29 (1970) pp 471-481.

[34] **Gilbert, P.F.C.,** "Iterative methods for three-dimensional reconstruction of an object from its projections", J. Theo. Biol. 36 (1972) pp 105-117.

[35] **Anderson, A.H., and Kak, A.C.,** "Simultaneous algebraic reconstruction technique (SART): a superior implementation of the ART algorithm", Ultrason. Imaging 6 (1984).

[36] **Lent, A.,** "A convergent algorithm for maximum entropy image reconstruction with a medical X-ray application", Proc. SPIE Image Analysis and Evaluation, R. Shaw, ed (1977) pp 249-257.

[37] **Bracewell, R.N., and Riddle, A.C.,** "Inversion of fan beam scan in radio astronomy", Astrophysics J. 150 (1967) pp 427-434.

[38] **Ramachandran, G.N., and Lakshminarayan, A.V.,** "Three-dimensional reconstruction from radiographs and electron micrographs: Application of convolution instead of Fourier transform", Proc. Natl. Sci. Acad. USA, 68 (1970) pp 2236-2240.

[39] **Hounsfield, G.N.,** "Computerized transverse axial scanning tomography, Part-I Description of the system", British Journal of Radiology, 46 (1973) pp 1016-1022.

[40] **Verhoeven, D.,** "Multiplicative algebraic computed tomographic algorithms for the reconstruction of multidimensional interferometeric data", Opt. Eng. 32 (1993) pp 410-419.

[41] **Gordon, R., Herman G.T.,** "Three-dimensional reconstruction from projections: A review of algorithms", Int. Rev. Cytol, 38 (1974) pp 111-115.

[42] **Natterer, F.,** The mathematics of computerized tomography, John Wiley, New York (1986).

[43] **Herman, G. T.,** Image reconstruction from projections, Academic Press, New York (1980).

[44] Censor, Y., "Finite series-expansion reconstruction methods", Proceedings of the IEEE, 71, No 3, (1983) pp 409-419.

[45] Debasish, M., "Experimental study of Rayleigh-Benard convection using interferometric tomography", PhD, Thesis, Nuclear Engineering and Technology Programme, Indian Institute of technology Kanpur, April 1998.

[46] Stewart, B. H. and Wendroff, B., "Two-phase flow: models and methods", J. Computational Phys. 56 (1984) pp 363-409.

[47] Buono, S., " Review of Thermal and Physical properties of Pb-Bi and other heavy Liquid Metals", First Meeting of the Benchmark Working Group on heavy liquid Metal Thermal Hydraulics, June 29-30, 1999, CERN, Geneva.

[48] Reid, C. R., Prausnitz, M. J., and Poling, E. B., "The Properties of Gases and Liquids", Fourth Edition, Mc-Graw-Hill Book Company (1986).

[49] Perry, R. H., Green, D., and Maloney, J. O., eds., PERRY'S CHEMICAL ENGINEERS' HANDBOOK, 6th Edition, Mc-Graw Hill Book Company, New York, 1984.

[50] J. Radon, "Uber die bestimmung von Funktionen durch ihre Integralwerte langs gewisser Mannigfaltigkeiten", Berichte Sachsische Akademie der Wissenschaften Leipzig, Math.-Phys. Kl., (1917), pp 262-267.

[51] Liles, R. D., and Reed, H. Wm., "A Semi-implicit Method for Two-phase Fluid Dynamics", J. Computational Phys. 26 (1978) pp 390-407.

52] Hirt, W. C., Amsden, A. A., and Cook, L. J., "An Arbitrary Lagrangian-Eulerian Computing Method for All Flow Speeds", J. Computational Phys. 14 (1974) pp 227-253.

APPENDIX A

Implementation of optimization reconstruction algorithms

A.1 Minimization of energy through Lagrangian multiplier optimization technique

The ith projection, which is a path integral, is approximated as

$$P_i = \sum_{j=1}^{N} w_{i,j} f_j \qquad i = 1, \ldots\ldots, M \qquad \text{(A.1.1)}$$

Minimum energy functional is defined as

$$F = \sum_j f_j^{\,2} \qquad\qquad\qquad \text{(A.1.2)}$$

Now based upon Lagrangian multiplier optimization technique,

$$F = -\sum_j f_j^{\,2} - \sum_{i=1}^{M} \lambda_i \left[\sum_{j=1}^{N} w_{i,j} f_j - P_i \right]$$

Here, λ_i are M unknown Lagrangian multipliers.

$$\frac{\partial F}{\partial f_j} = -2 f_j - \sum_{i=1}^{i=M} \lambda_i w_{i,j} = 0 \qquad \text{(A.1.3)}$$

$$f_j = -\frac{1}{2} \sum_{i=1}^{i=M} \lambda_i w_{i,j} \qquad \text{(A.1.4)}$$

Substituting Eq-(A.1.4) in Eq-(A.1.1) and simplifying

$$\sum_{i=1}^{i=M} \lambda_i \sum_{j=1}^{N} w_{i,j} w_{k,j} = -2 P_k \qquad \text{(A.1.5)}$$

Eq-(A.1.5) is a system of linear equations with the multipliers λ_i as unknown. This set of equations can be solver through Gauss-Seidel method for λ_i, and thereafter using λ_i, field can be reconstructed.

A.2 Maximization of entropy through Lagrangian multiplier optimization technique

Maximum entropy functional is defined as

$$F = -\sum_j f_j \ln(f_j) \tag{A.2.1}$$

Now based upon Lagrangian multiplier optimization technique for optimization of a function under some constraint,

$$F = -\sum_j f_j \ln(f_j) - \sum_{i=1}^{M} \lambda_i \left[\sum_{j=1}^{N} w_{i,j} f_j - P_i \right] \tag{A.2.2}$$

Here, λ_i are M unknown Lagrangian multipliers.

$$\frac{\partial F}{\partial f_j} = -\left(1 + \ln(f_j)\right) - \sum_{i=1}^{i=M} \lambda_i w_{i,j} = 0 \tag{A.2.3}$$

On simplification,

$$f_j = \exp\left(1 - \sum_{i=1}^{i=M} \lambda_i w_{i,j}\right) \tag{A.2.4}$$

Now putting f_j from Eq-(A.2.4), in Eq-(A.1.1),

$$\sum_{j=1}^{j=N} w_{i,j} \prod_{i=1}^{i=M} \left(\exp\left(-\lambda_i w_{i,j}\right)\right) = P_i \exp(1) \tag{A.2.5}$$

Replacing $\exp(-\lambda_i) = x_i$ in Eq-(A.2.5),

$$\sum_{j=1}^{j=N} w_{i,j} \prod_{i=1}^{i=M} (x_i)^{w_{i,j}} = P_i \exp(1) \tag{A.2.6}$$

Assuming,

$$g_i(x_i) = \sum_{j=1}^{j=N} w_{i,j} \prod_{i=1}^{i=M} (x_i)^{w_{i,j}} \tag{A.2.7}$$

$$g_i(x_i) = P_i \exp(1) \tag{A.2.8}$$

Now Eq-(A.2.6), can be solved by Gauss-Seidel method after linearization using truncated Taylor series expansion,

Let $x_i^{(1)}$ be the first guess for the solution set $x_i^{(n)}$.

$$P_i \exp(1) = g_i(x_i) = g_i(x_i^{(1)}) + \left(\frac{\partial g_i}{\partial x_1}\right)_{x_i^{(1)}} (x_1^{(2)} - x_1^{(1)}) + \left(\frac{\partial g_i}{\partial x_2}\right)_{x_i^{(1)}} (x_2^{(2)} - x_2^{(1)}) + \dots\dots$$

$$\dots\left(\frac{\partial g_i}{\partial x_M}\right)_{x_i^{(1)}} (x_M^{(2)} - x_M^{(1)}) \tag{A.2.9}$$

Now using Eq-(A.2.9) $x_i^{(2)}$ can be calculated, and then Lagrangian multipliers to calculate field values.